Mechanical compaction of crustal analogs made of sintered glass beads: the influence of porosity and grain size

Lucille Carbillet, Michael J Heap, Patrick Baud, Fabian B Wadsworth, Thierry Reuschle

Mechanical compaction of crustal analogs made of sintered glass beads: the influence of porosity and grain size

Lucille Carbillet[1], Michael J. Heap[1], Patrick Baud[1], Fabian B. Wadsworth[2], Thierry Reuschlé[1]

[1]Université de Strasbourg, CNRS, ENGEES, Institut Terre et Environnement de Strasbourg, UMR 7063, 5 rue René Descartes, Strasbourg F-67084, France

[2]Department of Earth Sciences, Durham University, Science Labs, Durham, United Kingdom

Corresponding author: Lucille Carbillet (lcarbillet@unistra.fr)

Key Points:

- The mechanical compaction behavior of monodisperse sintered glass bead samples is similar to that of well-sorted monomineralic sandstones
- During triaxial compression at high confining pressure, discrete compaction bands developed in a synthetic sample with a porosity of 0.35
- All else being equal, increasing grain diameter from 0.2 to 1.15 mm decreases the stress to reach C* by more than a factor of two

Abstract

The fundamentals of our understanding of the mechanical compaction of porous rocks stem from experimental studies. Yet, many of these studies use natural materials for which microstructural parameters are intrinsically coupled, hampering the diagnosis of relationships between microstructure and bulk sample behavior. To probe the influence of porosity and grain size on the mechanical compaction of granular rocks, we performed experiments on synthetic samples prepared by sintering monodisperse populations of glass beads, which allowed us to independently control porosity and grain diameter. We conducted hydrostatic and triaxial compression tests on synthetic samples with grain diameters and porosities in the ranges 0.2-1.15 mm and 0.18-0.38, respectively. During hydrostatic compaction, sample porosity decreased suddenly and substantially at the onset of inelastic compaction due to contemporaneous and extensive grain crushing, a consequence of the monodisperse grain size. During triaxial tests at high confining pressure, our synthetic samples failed by shear-enhanced compaction and showed evidence for the development of compaction bands. Critical stresses at the onset of inelastic compaction map out linear-shaped yield caps for the porosity-grain diameter combinations for which the critical stress for inelastic hydrostatic compaction is known. Our yield caps reinforce the first-order importance of porosity on the compactive yield strength and show, all else being equal, that grain size also exerts a first-order control and should therefore be routinely measured. Our study further reveals the suitability of sintered glass beads as analogs for crustal rocks, which facilitate the study of the deconvolved influence of microstructural parameters on their mechanical behavior.

Plain Language Summary

Porous rocks that form the shallow part of the Earth's crust are submitted to pressure conditions under which they deform by compaction, i.e., their porosity is reduced. Our understanding of the compaction stems primarily from laboratory experiments conducted on samples of natural rocks. Yet, because the internal structure of natural materials is complex, studying of the influence of structural parameters in isolation, such as porosity and grain size, on the way rock compacts is limited. To tackle this issue, we conducted compression tests on synthetic samples made of fused glass beads for which we could control porosity and grain size. When the pressure on the

synthetic rocks is increased uniformly in all directions, a threshold pressure, characteristic of the rock strength, is reached beyond which they compact suddenly and substantially. When a differential stress is imposed on the synthetic rocks, discrete bands of lower porosity are observed. We show that porosity and grain size exert a first-order control on the ability of the synthetic rocks to resist compaction. All else being equal, if the grain size is divided by five, the pressure beyond which the sample will deform by irreversible compaction is multiplied by more than two. Further, our synthetic samples are good analogs for natural rocks such as sandstones and tuffs and our results therefore have broad applications, from reservoir compaction and subsidence to the destabilization of volcanoes.

1 Introduction

The mechanical compaction of porous materials is an important process in the Earth's crust. It is one of the main deformation mechanisms of lithification, diagenesis, fault growth, and/or sealing, and plays a key role in many processes in sedimentary settings such as reservoirs, aquifers, and basins (Bjørlykke, 2006; Guéguen & Boutéca, 2004; Taylor et al., 2008), and in volcanic settings (Farquharson et al., 2017; Grunder & Russell, 2005; Quane et al., 2009). Understanding the phenomenology and micromechanics of compaction rests upon the ability to characterize the evolution of microstructure through compactant deformation. To predict the occurrence and extent of mechanical compaction, knowledge of the relationship between rock microstructural attributes and bulk mechanical properties is crucial. Indeed, the effective macroscopic properties of heterogeneous materials such as crustal rocks intricately depend on the phases present, their volume fraction, their spatial distribution, and their properties (e.g., Torquato, 2002). Therefore, relating microstructural attributes of porous rock to bulk properties has been the focus of numerous studies in the past decades, the majority of which relied on direct experimental measurements or numerical simulations (Blair et al., 1993; Doyen, 1988; Eberhart-Phillips et al., 1989; Ghazvinian et al., 2014; Schöpfer et al., 2009; Scott & Nielsen, 1991).

As early as 1990, it had already been suggested the two principle microstructural controls on the mechanical and hydraulic properties of sedimentary rocks were (1) porosity and (2) grain size (Bourbie & Zinszner, 1985; Paterson & Wong, 2005; Rutter & Glover, 2012; Zhang et al., 1990). Broadly speaking, an increase in rock porosity causes a decrease in strength (e.g., Baud et al.,

2014; Chang et al., 2006) and an increase in permeability (Bernabé et al., 2003; Dardis & Mccloskey, 1998). In detail, porosity also exerts an influence on the type of failure that can result from the application of crustal stresses (i.e., brittle or ductile). Low-porosity rock will remain brittle even under a wide range of pressure conditions (analogous to depth), whereas high-porosity rock will only behave in a brittle manner at relatively low-pressure and will transition to ductile behavior at high-pressure (Wong et al., 1997; Wong & Baud, 2012). Alongside the influence exerted by porosity, grain size has also been the target of an increasing number of experimental studies which demonstrated its controlling influence on mechanical and hydraulic properties (Atapour & Mortazavi, 2018; Schultz et al., 2010; Wasantha et al., 2015). However, when considering porosity and grain size, one usually refers to average values for the bulk volume of samples. As pores and grains are not always homogeneously distributed, a more accurate way to describe microstructure is to use pore and grain size distributions. Grain size distribution in lithified sedimentary rocks is also known to influence the mechanical behavior and failure mode (Guéguen & Fortin, 2013; Weng & Li, 2012; Xu et al., 2020), notably the possible development of compaction localization at high effective pressures (Baud et al., 2004). Assuming that grain crushing initiates by Hertzian fracture at grain contacts, Zhang et al. (1990) proposed a micromechanical model predicting the stress required to achieve grain crushing using porosity and grain size. While the model by Zhang et al. (1990) is in basic agreement with the existing data set, Rutter and Glover (2012) suggested that data for sandstones would be better described by a different empirical law. Moreover, the scatter on compiled experimental data remains large (Baud et al., 2014; Chang et al., 2006). Indeed, trends in plots of strength as a function of porosity or grain size are complicated by the fact that other microstructural parameters, such as pore size and shape, their distributions, or matrix composition, change together with porosity and grain size. For example, a decrease in porosity is often associated with an increase in the proportion of cement, that, if located along grain boundaries, can greatly increase the strength of granular materials (Baud et al., 2017; David et al., 1998; de Bono et al., 2015; Haeri et al., 2005; Yin & Dvorkin, 1994). These complexities arise from the fact that the influence of porosity, grain size, and these other microstructural considerations are all inter-connected and that ultimately a fruitful way forward would be to find a method by which they can be deconvolved and studied in isolation.

The uncertainty ensuing from the strong coupling between microstructural parameters, the inherent variability from sample to sample and the heterogeneity of natural materials limits the extent to which experimental studies can draw definitive conclusions about the influence of specific microstructural attributes on the mechanical properties of natural materials. To tackle this issue, several strategies could be considered: experiments using particularly simple materials occurring with a broad range of porosity such as Fontainebleau sandstone (Saadi et al., 2017; Sulem & Ouffroukh, 2006) or Leitha limestone (Baud et al., 2017); simulations using numerical samples (Schöpfer et al., 2009; Weng & Li, 2012); or experiments using synthetic samples (Bouzidi & Schmitt, 2012; Castagna & Backus, 1993; Chapman et al., 2018; David et al., 1998; Plona et al., 1980). In this study, we chose to follow the rationale of Berge et al. (1995), Guyon et al. (1987), and Wadsworth et al. (2016) who proposed sintered soda-lime silica glass beads as suitable analogs for granular crustal rocks, such as sandstones and tuffs. Silicate glass compositions have been extensively studied and data pertaining to their properties have been gathered in handbooks for various applications (e.g., Bansal & Doremus, 2013). The elastic properties of soda-lime silica glass are comparable to those of granular sedimentary and volcanic rocks (Berge et al., 1995; Vasseur et al., 2016). Additionally, in nature, grains that go through the different steps of diagenesis and form variably porous upper crust material are well approximated, to a first order, by sintering beads. Viscous sintering of glass beads then allows for the reproduction of the granular to non-granular transition and the preparation of synthetic rocks of pre-determined final porosity and grain size (Wadsworth et al., 2016).

In this paper, we present results of a suite of mechanical tests performed on synthetic samples made of monodisperse distributions of glass beads. After describing the preparation technique and the intact microstructure of our synthetic samples, we present the mechanical data and the associated failure mode. These results are discussed, and we will focus on the following questions. Mechanically speaking, how do the sintered glass beads samples compare with natural sandstones? Quantitatively, what is the influence of grain size and porosity on mechanical compaction? Considering the importance of compaction bands in the fields of rock mechanics, hydrology, and geology, could this failure mode be reproduced in synthetic samples?

2 Preparation and characterization of the synthetic samples

2.1 Viscous sintering of monodisperse populations of glass beads

When heated above the glass transition temperature interval, glass beads become viscous droplets. If these glass beads are packed together when heated then, as they transition from glass beads to viscous droplets, they can interact and coalesce in a process referred to as viscous sintering (Frenkel, 1945; Mackenzie & Shuttleworth, 1949; Wadsworth et al., 2016). The dominant consequence of viscous sintering is that the porosity is reduced with time. Because it is temperature-activated, this process has advantages for producing idealized porous materials. A desired packing arrangement, or grain size distribution can be determined in the cold, room temperature state, and then via heating, viscous sintering processes can be used to evolve that state to lower porosities.

Viscous sintering is driven by interfacial tension between the glass beads and the interstitial gas between the beads (Kuczynski, 1949). During viscous sintering, an initial system of viscous droplets evolves with time through two main stages: (1) the growth of necks between droplet-droplet pairs that share a contact (Frenkel, 1945), and (2) the shrinkage and closure of the pores between the droplets (Mackenzie & Shuttleworth, 1949). The initial system of viscous spherical droplets and interstitial pores evolves into a system of isolated pores within a viscous liquid continuum. That is, the end-state (gas in a liquid) is the inverse of the starting state (liquid in a gas) (Wadsworth et al., 2017). In practice, in order to reach a desired porosity in a desired time for a given grain size of glass bead, we control the temperature of synthesis (Wadsworth et al., 2016). The effect of changing the grain size is to change the pore size between the grains; therefore the ability to tweak the grain size of the starting glass bead population allows us to control the pore size distribution independently from the porosity, effectively deconvolving these structural controls.

Table 1. Chemical composition of glass beads (provided by manufacturer) used in this study. N.b. All wt% are recalculated to 100% disregarding the minor effect of loss on ignition.

Oxide	**SiLiBeads (wt%)**	**SpheriGlass (A-Glass) (wt%)**
SiO_2	72.95	72.5

Na_2O	13.08	13.7
CaO	9.06	9.8
MgO	4.25	3.3
Al_2O_3	0.58	0.4
FeO/Fe_2O_3	-	0.2
K_2O	-	0.1

We prepared three sets of samples using monodisperse populations of glass spheres of diameter between 0.15 and 0.25 mm (Spheriglass A-glass 1922 from Potters Industries Inc.), 0.4 and 0.6 mm (SiLibeads Glass beads type S 5218-7), or 1 and 1.3 mm (SiLibeads Glass beads type S 4504) of similar chemical composition (Table 1). The corresponding grain diameter distributions are presented in Figure 1(a). The synthetic rocks were prepared as blocks from which samples were cored. For each block, a monodisperse distribution of beads was poured into a ceramic tray of dimensions 205 × 125 × 50 mm. The tray was then manually shaken to flatten out the beak pack surface and then placed inside an electric box furnace (L9/11/SKM by Nabertherm). The box furnace was set to heat at a constant rate of 3 °C.min-1 to 680 °C, which is above the glass transition onset temperature of 549 °C provided by the manufacturer (similar for both bead type; Table 1). The peak sintering temperature was maintained constant for 1 to 12 hours depending on the target final porosity (longer times result in lower porosity). The tray was moved to 180° of its initial position halfway through the dwell to reduce the heterogeneity of the sintered block that may arise when the temperature distribution in a furnace is not even. After being held constant for a fixed time, the temperature in the furnace was lowered to 500 °C at a cooling rate of 1 °C.min-1 and finally decreased to ambient temperature at a cooling rate of 3 °C/min. This cooling workflow was designed to minimize thermal microcracking. 20 mm-diameter cylindrical samples were cored along the horizontal axis of the resulting sintered block to minimize gravity induced porosity gradients along the axis of the samples. These samples were then cut and precision-ground to a nominal length of 40 mm.

185 ## 2.2 Description of the sintered glass beads samples

186 A photograph of one of the synthetic samples is provided as Figure 1(b). Insights into the
187 microstructure of the synthetic samples were gained using polished thin sections observed under
188 a scanning electron microscope (SEM) (Figure 1(c)(d)). The SEM images were acquired on a
189 polished slice of a sample with a porosity of 0.35 and a mean grain diameter of 0.2 mm. As
190 predicted by the Frenkel model, adjacent beads are connected by a neck and pore space remains
191 between the bonded grains (Figure 1(d)). The lowest porosity obtained in this study is 0.22.
192 Therefore, all our samples are in the range between high porosity – close to the initial packing
193 porosity where incipient sintering has only formed necks – and intermediate porosity – where
194 sintering has progressed and begun to close the pore network. Our study does not encompass low
195 porosity synthetic rocks which would exhibit pore structures close to isolated pores in a glass
196 medium (the equilibrium porosity at the end of sintering is 0.03; Wadsworth et al., 2016) .
197 Thus, all our samples are in the upper range of porosity encompassed by natural granular rocks.
198 While a material is only truly granular when the individual grains can move relative to one
199 another (which is the case for the glass beads prior to sintering), our synthetic rocks are close to
200 that granular end member case. The microstructure of an assembly of soda-lime silica glass
201 spheres that underwent densification by sintering to a more advanced stage have been imaged in
202 2D by Vasseur et al. (2016) and continuously in 3D by Wadsworth et al. (2017), who performed
203 X-ray computed-tomography. These studies showed that the topological inversion of the viscous
204 system takes place continuously through sintering, hence allowing for the construction of a
205 unified physical description for the evolution of porosity and permeability during viscous
206 sintering.
207 Although statistically homogeneous, the granular materials prepared here by sintering glass
208 spheres present heterogeneities on the scale of 2-3 grains. Indeed, SEM images of intact samples
209 reveal small heterogeneities in the pore size distribution (Figure 1(c)). As our preparation
210 workflow allows for controlling the diameter of the grains and the degree of polydispersivity but
211 not for designing the exact nature and structure of the porous space, some porous patches, whose
212 width can reach 0.4 mm, can be observed in our intact samples (Figure 1(c)). Using square
213 windows of 0.8 mm of edge-length and of 2mm of edge-length, 2D porosity measurements were
214 performed on SEM images of intact samples (using ImageJ). The square window with an edge-
215 length of 2 mm ensures that the measured area contains at least 10 glass beads in any one

direction, to ensure a representative element volume (REV), and the square window with an edge-length of 0.8 mm allows us to better understand whether there are variations in porosity on a smaller scale. Figure 1(e) presents histograms of the distributions of 2D porosity measurements obtained for the zoomed-out SEM image in Figure 1(c). While porosity measurements performed in the larger window provide a monomodal distribution closely-clustered around 0.35, porosity measurements performed in the smaller window yield local values up to 0.42 in a sample with an average porosity of 0.35. We refer to these volumes as porosity clusters. In addition, the absence of cement is accompanied by heterogeneities in the local grain contacts geometry, as previously reported by den Brok et al. (1997). Sintered porous materials are random heterogeneous but isotropic porous media in terms of their microstructure, where we use 'heterogeneous' to refer to the lack of structural order. However, our samples are homogeneous in the sense that the random variation in the microstructure occurs on length scales much less than the sample lengths.

3 Experimental procedures

To study mechanical compaction using synthetic samples, we conducted a suite of mechanical tests on sintered glass bead samples. We performed hydrostatic and conventional triaxial compression experiments. During hydrostatic experiments the principal stresses are equal in all directions, i.e., the state of stress is $\sigma_1 = \sigma_2 = \sigma_3$. During triaxial experiments, an axial stress is superimposed onto a hydrostatic pressure. The principal stress parallel to the axis of the sample is higher than the principal stresses normal to this axis, i.e., the state of stress is $\sigma_1 > \sigma_2 = \sigma_3$. Although we focus here on compaction, we performed a few triaxial tests at relatively low pressure to identify the brittle-ductile transition. A summary of all our experiments is provided in Table 2. The solid density of glass beads was determined using a helium pycnometer (Micromeritics AccuPyc II 1340) prior to and after sintering at 680°C. We found that the solid density of the glass beads, 2.49 g/cm3, was unchanged following exposure to 680°C. As we know the solid density of the glass beads, porosity was derived from the dimensions and the mass of the samples. The mean error associated with the porosity measurement is 0.005 (Table 2). The permeability of the samples was measured prior to deformation using a benchtop gaz (nitrogen) permeameter. Permeability was measured under a confining pressure of 1 MPa using the steady-state method (following the method detailed in Heap et al., 2017). All experiments were conducted at the Ecole et Observatoire des Sciences de la Terre (EOST) in Strasbourg

(France) following the procedure detailed by Baud et al. (2015). All samples underwent the same preparation before the experiments. First, the samples were encased in very thin (< 1 mm-thick) copper foil jackets to preserve bulk sample cohesion following deformation (so that thin sections could be prepared) and to avoid disking. The samples were then dried in a vacuum oven at 40 °C for at least 48 hours and then vacuum-saturated with deionized water. Before each test, the sample to be deformed was positioned between two steel end-caps – the bottom one of which has a concentric hole at the center for fluid access to the pore pressure system. In addition, the bottom endcap was separated from the sample by a thin highly permeable filter, made from coffee filter paper, to prevent broken beads from infiltrating the pore pressure piping during the experiments. Viton® tubing was used to separate the sample from the confining pressure system. All experiments were performed at room temperature on water-saturated samples. Computer-controlled stepping motors were used to independently regulate the confining pressure, pore fluid pressure and axial stress. Data were acquired with a sampling period of 10s for hydrostatic experiments and 1s for triaxial compression experiments.

Table 2. Experimental conditions and mechanical data of the synthetic samples tested in this study. Triaxial tests were conducted at nominal strain rates of 10^{-5} s^{-1}.

Sample	Porosity	+/- (mean error = 0.005)	Confining pressure P_c (MPa)	Pore pressure P_p (MPa)	Effective pressure $P_{eff} = P_c - P_p$ (MPa)	Peak stress σ_v		Yield stress C*	
						P (MPa)	Q (MPa)	P (MPa)	Q (MPa)
mean grain diameter 1.15 mm									
1814	0.181	0.004	-	-	0	10	30	-	-
1812	0.183	0.003	40	10	30	-	-	92	185
1816	0.189	0.004	60	10	50	-	-	115	194
1412	0.271	0.005	30	10	20	38	55	-	-
1414	0.265	0.005	70	10	60	-	-	80	59
1419	0.262	0.005	100	10	90	-	-	105	45
1413	0.269	0.005	130	10	120	-	-	132	35
1411	0.271	0.005	160	10	150	-	-	159	28
114012	0.294	0.006	-	-	0	1.4	4.3	-	-

114013	0.302	0.006	40	10	30	36	17	-	-
114011	0.308	0.006	70	10	60	74	43	-	-
1314	0.294	0.006	100	10	90	-	-	102	35
1313	0.303	0.006	130	10	120	-	-	128	23
114016	0.294	0.006	-	10	hydrostatic	-	-	*P**	
								156	0
					mean grain diameter 0.5 mm				
2317	0.255	0.005	-	-	0	10	31	-	-
23111	0.249	0.005	40	10	30	74	132	-	-
2316	0.256	0.005	70	10	60	-	-	92	97
2318	0.258	0.005	110	10	100	-	-	133	100
2313	0.263	0.005	160	10	150	-	-	177	80
2314	0.256	0.005	190	10	180	-	-	200	60
22114	0.299	0.006	-	-	0	20	7	-	-
2218	0.302	0.006	30	10	20	-	-	40	59
27312	0.304	0.006	50	10	40	-	-	61	63
22111	0.292	0.006	70	10	60	-	-	83	70
27314	0.295	0.006	90	10	80	-	-	99	58
27315	0.294	0.006	110	10	100	-	-	117	52
22213	0.301	0.006	120	10	110	-	-	125	45
27313	0.299	0.006	130	10	120	-	-	133	39
2213	0.299	0.006	150	10	140	-	-	152	36
2217	0.296	0.006	170	10	160	-	-	168	23
27311	0.295	0.006	-	10	hydrostatic	-	-	P*	
								173	0
					mean grain diameter 0.2 mm				

31012	0.225	0.005	-	-	0	20	59	-	-
31713	0.220	0.004	40	10	30	-	-	87	172
31013	0.222	0.004	70	10	60	-	-	130	212
37	0.226	0.005	90	10	80	-	-	150	212
31113	0.256	0.005	70	10	60	-	-	109	147
31110	0.266	0.006	130	10	120	-	-	177	170
311	0.262	0.005	160	10	150	-	-	200	150
31114	0.255	0.005	190	10	180	-	-	225	135
3813	0.300	0.005	40	10	30	68	115	-	-
3814	0.307	0.006	70	10	60	-	-	92	95
3413	0.305	0.006	130	10	120	-	-	146	77
3411	0.299	0.006	190	10	180	-	-	200	61
3311	0.346	0,007	30	10	20	-	-	35	46
3612	0.353	0.008	50	10	40	-	-	58	55
339	0.351	0.008	70	10	60	-	-	74	42
3314	0.356	0.007	90	10	80	-	-	91	33
3312	0.357	0.008	-	10	hydrostatic	-	-	*P**	
								118	0
3710	0.385	0.009	40	10	30	-	-	37	22
379	0.387	0.009	50	10	40	-	-	46	19
3711	0.385	0.007	60	10	50	-	-	54	13
3712	0.382	0.007	-	10	hydrostatic	-	-	*P**	
								69	0

For both hydrostatic and triaxial compression tests, the confining pressure P_c (kerosene) and the pore fluid pressure P_p (deionized water) were first slowly increased to their target values using servo-controlled pumps (see Table 2 for values). A fixed pore fluid pressure P_p of 10 MPa was used for all experiments and we assume a simple effective pressure law $P_{eff} = P_c - P_p$, operative

for rock failure under static conditions, as shown for sandstones by Baud et al. (2015) in the brittle and ductile regimes. For the hydrostatic tests, the effective pressure P_{eff} was increased in small steps from its initial value of 2 MPa until the critical stress state for the onset of grain crushing P* (Zhang et al., 1990), or the upper pressure limit of the press (P_c =200 MPa), was reached. We waited for microstructural equilibrium at each step before increasing the confining pressure further. To do this, we assume that microstructural equilibrium was achieved when the rate of the pore volume change (recorded by monitoring the displacement of the piston in the pore pressure intensifier) was lower than 10^{-2} s^{-1}. The amount by which P_{eff} was increased at each step varied from 1 to 10 MPa depending on the time necessary to reach microstructural equilibrium at the previous step. For triaxial experiments, once the targeted effective pressure P_{eff} was reached (i.e., hydrostatic pressurization, see Table 2 for values), the system was left to equilibrate until the pore fluid change was lower than 10^{-2} s^{-1}. Then, at constant P_{eff}, the sample was loaded as the upper piston was lowered at a fixed servo-controlled rate corresponding to a nominal strain rate of 10^{-5} s^{-1}. Considering the range of permeabilities of the synthetics (from 10^{-13} to 10^{-11} m^2, measured at a P_c of 1 MPa), the strain rate applied during triaxial compression was low enough to ensure drained conditions (i.e., the product of the strain rate and the Darcy timescale $Da = t_D\varepsilon = \mu_f L^2/(k\Delta P)$ is much less than unity (Heap & Wadsworth, 2016)).

During all tests, a linear variable differential transformer (LVDT) monitored the position of the upper piston with an accuracy of 0.2 µm, thus giving access to displacement, and a pressure probe in the axial pressure circuit provided a measurement of the applied axial force. Using the initial dimensions of the sample, axial stress and strain were obtained. Porosity change was provided by the conversion of the pore volume change given by the displacement of the piston in the pore pressure intensifier (the system was calibrated to take into account the compressibility of the pore fluid (water)). Finally, acoustic emission (AE) activity was recorded using a USB AE Node from Physical Acoustics and a piezoelectric transducer (a micro80 sensor from Physical Acoustic with a bandwidth of 200-900 kHz) attached to the lower piston. AE activity was monitored using the software AEwin and we set the detection threshold for an AE hit at 28 dB. The AE energy is determined by AEwin as the area under the received waveform. Experiments were stopped after the samples were unloaded at the same servo-controlled rate as loading and the pressures removed slowly so as not to damage the samples. For experiments conducted in the brittle regime, samples were unloaded following macroscopic failure. In the ductile regime,

samples were deformed up to a 4% axial strain if mechanical data indicated strain localization (i.e., if there were small stress drops in the mechanical data) and up to 6% if not. Based on previous studies on natural rocks (Baud et al., 2004), these strains are considered suitable for subsequent observation of microstructural deformation features. To gain insights into the microstructure, polished thin sections were prepared using selected deformed samples and micrographs of the thin sections were obtained using a SEM.

4 Mechanical data

In this study, compressive stress and compactive strain, i.e., shortening for axial strain and decreasing volume for volumetric strain, will be conventionally taken as positive. The maximum and minimum applied principal compressive stresses are referred to as σ_1 and σ_3, respectively, the differential stress as $Q = \sigma_1 - \sigma_3$ and the effective mean stress as $P = (\sigma_1 + 2\sigma_3)/3 - P_p$.

4.1 Results of the hydrostatic and triaxial tests

Representative data for the mechanical response of sintered glass bead samples to hydrostatic loading are presented in Figure 2. The hydrostatic experiment was conducted on a synthetic sample with a porosity and mean grain diameter of 0.38 and 0.2 mm (3714 in Table 2) and the mechanical data are plotted alongside the corresponding AE activity (dashed purple). The gray dashed curve in Figure 2 presents the mechanical data from an experiment performed on a sample with a very similar porosity and the same grain diameter to show the reproducibility (3712 in Table 2). The porosity reduction in pourcentage corresponds to the absolute loss of porosity. In Figure 2, the hydrostats present the following characteristic phases. (1) The initial evolution of porosity with increasing effective pressure is non-linear. The duration of this first stage varies from sample to sample, as demonstrated by the difference between the black and the gray curves, and is positively correlated to porosity. (2) The second phase consists of a linear decrease of porosity as a function of increasing effective mean stress, which is characteristic of poroelastic behavior. Almost no AEs are recorded during the initial non-linear and linear portions of the hydrostatic experiment (Figure 2). However, a sudden increase in cumulative AE, associated with a sharp breaking point in the mechanical data, indicated as P*, marks the transition to (3) a third phase characterized by a large decrease in porosity (of about 0.1) at constant effective pressure. For siliciclastic rock, this inflection on the hydrostat followed by a

large porosity reduction is characteristic of inelastic compaction by delocalized grain crushing (Zhang et al., 1990), P* therefore represents the critical stress for the onset of grain crushing. After equilibrium of the system has been reached for the critical state of stress P*, further increase of the effective stress is accompanied by hardening. Samples submitted to hydrostatic loading (up to the maximum capability of the pressure cell; i.e., P_c = 200 MPa) presented effective pressure-porosity reduction curves similar to the hydrostats presented in Figure 2.

Triaxial compression experiments were conducted at effective pressures P_{eff} ranging from 20 to 180 MPa and, depending on the effective pressure P_{eff}, led to either brittle or ductile failure. A representative curve for the mechanical data and AE activity corresponding to failure by dilatancy and shear fracture formation (i.e., brittle behavior) is presented in Figure 3. The stress-strain curve can be divided into three parts. (1) First, the axial strain increases linearly with the differential stress and very few AEs are recorded. (2) Second, a sudden increase in the AEs accompanies a small decrease in the slope of the stress-strain curve, which corresponds to the onset of dilatancy (Figure 3). (3) Finally, as the AE bursts, the differential stress reaches a peak (marked as σ_v) and then drops to a residual value. Among the synthetic samples deformed under triaxial conditions, samples of porosity below 0.26 demonstrated brittle behavior up to effective pressures of 30 to 60 MPa, depending on their grain diameter. The peak stresses σ_v for samples deformed in the brittle regime are compiled in Table 2.

Figure 4 shows the third type of mechanical data obtained in this study, i.e., mechanical data for triaxial tests conducted on synthetic samples at relatively high confinement and which failed by shear-enhanced compaction. On Figure 4, the stress-strain curve can be delimited into two main portions. (1) As we first load the sample, axial strain increases linearly with differential stress and no AEs are recorded. (2) Then, a subtle decrease in the slope of the stress-strain curve takes place as the AEs start to increase at the onset of shear-enhanced compaction C* (Wong et al., 1997). Finally, the stress-strain curve reaches a plateau punctuated by stress drops that correlate to spikes in the AEs. These stress drops are suggestive of the formation of compaction bands (Baud et al., 2004). All samples deformed in the range of effective pressures corresponding to shear-enhanced compaction demonstrated such stress drops, sometimes accompanied by strain hardening. The critical stresses C* for samples deformed in the ductile regime are compiled in Table 2.

An overview of the mechanical data collected for this study is presented in Figure 5. Mechanical data for triaxial experiments are compiled with their corresponding hydrostatic pressurization curves, for samples of porosity ranging from 0.18 to 0.38 and for mean grain diameters of 1.15 (blue), 0.5 (green) and 0.2 (orange) mm. At low and high effective pressures, the mechanical data present the phases described for Figure 3 and Figure 4, respectively. The mechanical data for triaxial compression follow the hydrostat in the poroelastic domain. The deviation from the hydrostat marks the transition to inelastic deformation, either by dilatancy (increase in porosity) or by shear-enhanced compaction (porosity reduction). Some samples deformed in a mode that cannot be easily defined as “brittle” or “ductile”. The mechanical data for the experiments performed at effective pressures of 30, 60, and 90 MPa in Figure 5(c) are representative of this hard-to-define failure mode, which we will refer to as transitional. For all the experiments, peak stresses and critical stresses were identified to map out the failure envelopes of our synthetic samples (Table 2).

4.2 Critical stress states: effect of porosity and grain size

For all experiments, critical stress values were identified in accordance with the failure mode (Figures 2, 3 and 4). Regarding experiments conducted in the brittle and transitional regime, critical stresses P and Q were respectively identified at the peak and at the first stress drop. For experiments conducted in the ductile regime, the stresses P and Q were identified at the deviation from the hydrostat, i.e., at the onset of shear-enhanced compaction C* (Figure 5). Table 2 includes all experiments for which the critical stresses could be clearly identified using mechanical data and AE measurements.

When plotted in the effective mean stress P - differential stress Q space, peak stresses map out the brittle failure envelope (open symbols) and C* values map out the compactive yield envelope (solid symbols). When it could be measured, P* anchors the yield envelope on the x-axis (P* could not be measured for all combinations of porosity and grain size due to the pressure limitations of the triaxial press). The experiments that exhibited a transitional failure mode exist where the brittle envelope meets the yield cap. Figure 6 presents a compilation of failure envelopes for our synthetic samples. Overall, several common features of the envelopes should be noted. First, brittle failure of these porous materials is restricted to a small area of the stress space. Second, regarding compactive yield caps, P and Q are linearly correlated, which is

particularly clear for the caps on Figure 6(c). Third, shear-enhanced compaction occurs over a wide range of stress states. For a given grain diameter, porosity is seen to influence compactive yield behavior. Broadly speaking, the higher porosity, the lower the stress that required for inelastic yield. For example, samples of mean grain diameter of 1.15 mm (Figure 6(a)) submitted to triaxial compression under an effective pressure of 120 MPa yielded at 23 and 35 MPa of differential stress for initial porosities of $\varphi = 0.30$ and $\varphi = 0.26$, respectively. For samples of mean grain diameter of 0.5 mm (Figure 6(b)), triaxial compression under an effective pressure of 100 MPa resulted in critical differential stresses of 100 MPa for $\varphi = 0.26$ compared to 52 MPa for $\varphi = 0.30$. Finally, for synthetic samples of mean grain diameter of 0.2 mm (Figure 6(c)) deformed at $P_{eff} = 60$ MPa, inelastic yielding took place at 223 MPa when $\varphi = 0.22$, 147 MPa when $\varphi = 0.26$, 95 MPa when $\varphi = 0.30$, and 42 MPa when $\varphi = 0.35$. In summary, increasing the porosity from 0.22 to 0.35 decreased the stress required for C* by more than a factor of five (Table 2).

All else being equal, grain diameter also exerts an important influence on the compactive behavior. Figure 7(a) and Figure 7(b) presents a compilation of caps for $\varphi = 0.30$ and 0.25-0.26, respectively, for three different mean grain diameters (1.15 mm in blue, 0.5 mm in green, and 0.2 mm in orange). For $\varphi = 0.25$-0.26 and $P_{eff} = 60$ MPa, shear-enhanced compaction started at 59, 97 and 147 MPa for monodisperse samples of 1.15, 0.5 and 0.2 mm of mean grain diameter respectively. For $\varphi = 0.30$ and $P_{eff} = 120$ MPa, C* was reached at 23, 39 and 77 MPa for samples of 1.15, 0.5 and 0.2 mm of mean grain diameter respectively. In summary, increasing the mean grain diameter from 0.2 to 1.15 mm decreased the stress required for C* by more than a factor of two (Table 2).

5 Microstructural observations

Representative SEM micrographs for the microstructure of a synthetic sample after hydrostatic compression to beyond P* are presented in Figure 8. The images correspond to a sample with an initial porosity and mean grain diameter of 0.357 and 0.2 mm (sample 3312; see Table 2), respectively, deformed up to a porosity reduction of 0.16. The corresponding mechanical data are presented in Figure 5(i). At the lowest magnification, the thin section shows extensive delocalized grain crushing. Zooms into the microstructure confirm that most grains were entirely crushed and that the resulting shards progressively filled the porosity as the sample compacted.

Uncrushed glass beads allow for the observation of cross-cutting microfractures propagating from grain to grain. On the basis of 2D image analysis (using ImageJ), the local final porosity was estimated. The least and most damaged areas yielded porosity values around 0.30 and 0.11, respectively.

Representative SEM for the microstructure of a synthetic sample triaxially deformed to beyond C* are presented in Figure 9. The images correspond to a sample with an initial porosity and mean grain diameter of 0.35 and 0.2 mm (sample 3314; see Table 2), respectively, triaxially deformed at an effective pressure of 80 MPa up to an axial strain of 3.5%. The corresponding mechanical data are presented in Figure 5(i). As suggested by the small stress drops punctuating the stress-strain curve beyond C* and the corresponding bursts of AE activity (Figure 5(i)), the sample contains evidence of compaction localization. Several discrete bands were observed in the upper and lower parts of the thin section, i.e., at the extremities of the sample, and one cross-cutting discrete band was observed in the middle (Figure 9). The compaction band in the middle is 2-5 grains wide – i.e., thickness of 0.4 to 1 mm – and is oriented normal to the direction to the maximum principal stress σ_1. Note that the band appears to avoid the porosity patches, and thus slaloms between them. A zoom on the band shows extensively fractured and compacted glass beads (Figure 9). Shards resulting from the fracturing and crushing fill the porosity within the band, reducing the porosity from 0.35 to approximately 0.27 (estimation based on 2D measurements on the SEM images using ImageJ). The grains are unaffected outside the compaction band, and the porosity was estimated using ImageJ to be similar to that measured in the laboratory (0.36).

6 Discussion

6.1 Suitability of sintered glass beads as crustal analogues

Synthetic granular rocks such as our sintered soda-lime silica glass beads provide a well-characterized two-phase medium for investigating mechanical processes in siliciclastic rock. Our motivation for using synthetic samples was to quantify the influence of individual microstructural parameters (e.g., porosity and grain diameter) on the mechanical behavior of granular rock by keeping all other parameters constant. In natural sandstones, for example, samples with different porosities may also be characterized by different grain and pore sizes and

446 distributions. However, understanding the mechanical behavior of sandstones using fused glass
447 bead synthetics hinges on the comparability of natural and synthetic sandstones. Before
448 discussing the suitability of sintered glass beads as analogs for crustal rocks, we will briefly
449 mention the differences between the microstructure of our synthetic samples and natural crustal
450 rocks. First, the grain size distribution of all the synthetic samples is monomodal and closely-
451 clustered (Figure 1a). Natural sandstones, for example, can be characterized by polydisperse
452 grain size distributions. Second, the grains in our synthetic samples are spherical and have
453 identical physical and mechanical properties, while natural sandstones often contain non-
454 spherical grains and different types of grains (e.g., quartz and feldspar). Finally, natural
455 sandstones can contain cement (e.g., clay cement between grains). Our synthetic samples do not
456 contain cement (Figure 1c and 1d). To compare our synthetic samples to natural sandstones, we
457 selected sandstones whose porosity and grain diameter lie in the range covered by our synthetic
458 samples (our porosity range is 0.18-0.38 and our grain diameter range is 0.2-1.2 mm). We chose
459 Boise sandstone (porosity of 0.35 and average grain radius 0.46 mm; Bedford et al., 2019; Zhang
460 et al., 1990), Idaho Gray sandstone (porosity of 0.36 and average grain radius 0.7 +/- 0.2 mm;
461 Bedford et al., 2019) and Bentheim sandstone (porosity of 0.23 and average grain radius 0.3 mm;
462 Klein et al., 2001). Bentheim sandstone is a monomineralic sandstone with a narrow grain size
463 distribution. Due to its homogeneous mineralogy and well sorted grain size, it has been used in
464 many rock deformation studies, notably on strain localization (Baud et al., 2004; Tembe et al.,
465 2006, 2008; Wong et al., 2001). It is therefore an ideal sandstone to compare with our synthetic
466 samples. We compiled mechanical data from hydrostatic and triaxial experiments conducted in
467 conditions similar to those imposed during experiments on the synthetic samples, i.e., at room
468 temperature on water-saturated samples at a fixed pore pressure of 10 MPa. In Figure 10, we plot
469 selected mechanical data from our database alongside mechanical data from hydrostatic
470 experiments (a) and triaxial experiments (b) conducted on Boise, Idaho Gray and Bentheim
471 sandstones.

472 Regarding the hydrostatic behavior. (Figure 10(a)), we first note that, during the initial loading
473 and increase of the effective pressure up to P*, Boise, Idaho Gray, and the synthetic sample with
474 a porosity of 0.35 present porosity reduction curves that are almost identical. The characteristic
475 “tail” at the beginning of the hydrostat is typically attributed to the closure of microcracks
476 (Walsh, 1965). Assuming our sintered glass beads do not contain microfractures at the beginning

of the hydrostatic pressurization, as indicated from our microstructural analysis of the intact material, we attribute the non-linear initial portion of the hydrostat to grain rotations and rearrangements, which is corroborated by the positive correlation between the size of the tail (i.e., the amount of compaction) and the porosity of the sample. Qualitatively speaking, the compaction curves evolve differently beyond P*. While a progressive inflection and strain hardening is observed for both Boise and Idaho Gray sandstones, P* manifests as a sharp breaking point beyond which the synthetic sample undergoes a porosity reduction of about 0.1 without hardening. Zhang et al. (1990) demonstrated that the first inflection in the hydrostat corresponds to the inception of grain crushing and that increasing the effective pressure beyond this point exacerbates the deformation. This gradual behavior is absent for the synthetic sample, which experiences extensive grain crushing and porosity loss at the state of stress just higher than P*. The observation of extensive grain crushing at a stress just above P* is similar to that reported for Bentheim sandstone, a rock that also contains a closely-clustered monomodal grain size distribution (Baud et al., 2006)(Figure 10(a)(c)). Examination of the microstructure showed that very few areas in the sample remained uncrushed (Figure 8). Contrary to most natural sandstones (e.g., Caruso et al., 1985), our synthetic rocks are composed of monomodal distributions of uniform grains of identical elastic properties. Thus, the force chains induced in the granular framework during loading are expected to be more homogeneously distributed in our monodisperse synthetic samples (Guéguen & Boutéca, 2004; Papadopoulos et al., 2018). As a result of this homogeneity, when the externally applied effective pressure reaches the critical value P*, the normal forces induced at the grain contacts must reach the critical value at the same time, and most grains are thus crushed at the same state of stress. Quantitatively, the effective stress at which the onset of grain crushing (P*) occurs is higher in our synthetic rock (120 MPa) than it is in Boise (75 MPa) and Idaho Gray (55 MPa) sandstones. Several differences between the synthetic and natural samples could be considered to explain the higher P* in the synthetic samples. First, Boise and Idaho Gray sandstone have a larger average grain diameter. Second, Boise and Idaho Gray sandstone contain minerals other than quartz that are characterized by lower values of fracture toughness, such as feldspar (Atkinson & Meredith, 1987). However, although the mineral composition of the two sandstones is very close, the P* of Boise sandstone is about 25 MPa higher than that of Idaho Gray sandstone (Figure 10(a)). Therefore, we

speculate that the much higher P* for the synthetic samples could arise from the difference in grain diameter (the smaller the grains, the stronger the sample).

We will now compare the behavior of natural sandstones with the one of our synthetic samples when subject to triaxial compression. Figure 10(b) presents mechanical data from triaxial tests conducted on a synthetic sample with a porosity of 0.3 (orange line) and on Bentheim sandstone (Baud et al., 2004) (black line) under an effective pressure of 120 MPa. Qualitatively, the stress-strain curves are very similar. Quantitatively, C* is about 50 MPa higher in Bentheim sandstone than in the synthetic sample and is likely the result of the difference in porosity and grain size (both higher for the synthetic sample). Beyond C*, the mechanical data for both samples show small stress drops, suggesting that the samples failed by development of compaction localization, as shown by Baud et al. (2004).

Although studies on the mechanical behavior of tuffs under hydrostatic and triaxial compression are comparatively rare (e.g., Heap et al., 2015a; Zhu et al., 2011), our new data for sintered synthetic samples are also relevant to welded granular materials. Indeed, in the case of welded tuffs – the product of the deposition of hot volcanic ash and lapilli – our samples are an exact analog, where volcanic welding and glass sintering are fundamentally the same dynamic process (Wadsworth et al., 2019). We note that in nature, welding of tuff can be associated with internally porous clasts, vesiculation or resorption, viscosity or temperature gradients, and shear, all of which can conspire to complicate microstructure relative to sintered glass beads, but that nevertheless, the broad theme of mechanical results given here are relevant in volcanic environments as well as other crustal scenarios.

6.2 Deconvolution of microstructural parameters

In nature, porosity is often related to grain diameter. However, numerous other parameters such as grain sorting, shape, orientation, location of cements, and the extent of compaction, can influence the bulk porosity of a porous rock (Rogers & Head, 1961; Scherer, 1987). One of the results of this multi-component control on porosity is that crustal rocks that show a low porosity are not necessarily composed of small grains and vice versa. In fact, crustal rocks span a wide range of porosity-grain size combinations and can demonstrate complex porosity-grain size relationships. For illustration, we have compiled the porosity and the mean grain diameter of 19 natural sandstones that have repeatedly been used in laboratory studies (Figure 11). Porosity

537 values are in the range 0.03-0.38 and mean grain diameter values are in the range 0.075-0.92 mm.
538 If we consider only this subset of natural sandstones, several observations can be made: (1) for
539 the few sandstones with a porosity higher than 0.25, the mean grain diameter varies over a range
540 twice as large as sandstones of lower porosity (0.2-0.9) and (2) for sandstones of porosity lower
541 or equal to 0.25, mean grain diameter is lower than 0.5 mm and clusters around 0.28 mm; such
542 that the grain size effect on porosity becomes attenuated as diagenesis progresses as pore and
543 pore throats are compacted. By compiling these data, we can conclude that (3) sandstones that
544 come from a single formation (see for example Buntsandstein, Fontainebleau or Boise
545 sandstones) can cover a large range in grain diameter and porosity, within which variations in
546 grain diameter appear to occur independently from variations in porosity and vice versa. For
547 example, the porosity of Fontainebleau sandstone can vary greatly (0.03-0.28), while the mean
548 grain diameter (0.250 mm) remains constant (Bourbie & Zinszner, 1985; Lindquist et al., 2000;
549 Louis et al., 2007). It is important to note that there is some bias in sample selection for
550 laboratory studies, such that crustal rocks with a low variability within a unit are favored so that
551 repeat measurements can be made (e.g., Menéndez et al., 1996). We can find that field studies
552 reported a much wider range of average grain size and porosity for sandstones, which can be
553 encountered as very fine-grained (0.0625 mm; Selley, 2004) and can grade up to very coarse-
554 grained and pebbly (2 mm; Selley, 2004), with well to poorly-sorted distributions and porosity
555 ranging over more than one order of magnitude 0.02-0.30 (e.g., Morrow, Nugget, Bartlesville,
556 and Grimsby sandstone; Nelson & Kibler, 2003). For instance, anomalously high porosities were
557 reported in a significant number of deeply-buried (> 4 km) reservoir sandstones worldwide (e.g.,
558 porosity in the range 0.24-0.40 in the Tertiary channel-fill sandstone, offshore west Africa; Bloch
559 et al., 2002).

560 Deconvolving structural parameters such as porosity and grain size is necessary to derive
561 definitive constraints on the micromechanics of compaction from experimental studies. Indeed,
562 while the importance of porosity in controlling yield strength is well-established for crustal rocks
563 (e.g., Wong & Baud, 2012), the independent effect of a change of grain or pore size is only
564 poorly investigated (Atapour & Mortazavi, 2018). As revealed when compiling grain diameter
565 and porosity for laboratory sandstones (Figure 11), it is possible that the approximate consistency
566 in the grain diameter has meant that its influence on compactive yield strength has been masked
567 in rock mechanics study thus far. Sintering glass beads has allowed us to effectively deconvolve

the effect of porosity and grain diameter and other microstructural factors, to parameterize specifically for their importance.

6.3 Influence of porosity and grain size on compactive yield

Our synthetic samples were designed and prepared to maximize microstructural homogeneity. Yet, they present heterogeneities in the porosity distribution and in the geometry of grain-to-grain contacts (Figure 1). Similar porosity clusters have been reported in Bleurswiller sandstone, the mechanical compaction of which has been investigated in several studies (Baud et al., 2015; Fortin et al., 2005, 2006; Tembe et al., 2008). These published works have demonstrated the importance of porosity clusters on the micromechanical processes leading to inelastic compaction. Indeed, while yield envelopes reported for natural sandstones are typically elliptical in shape (Baud et al., 2006; Guéguen & Fortin, 2013; Wong et al., 1997), Bleurswiller sandstone presents an approximately linear yield cap (Baud et al., 2015). The linear yield envelope of Bleurswiller was fitted by Baud et al. (2015) using a dual-porosity micromechanical model for cataclastic pore collapse. The pore collapse model, initially developed for dual-porosity carbonates, treats the pore size distribution as bimodal with the pore space divided into microporosity and macroporosity (i.e., a porosity cluster) (Zhu et al., 2010). Assuming the matrix into which porosity clusters are embedded fails according to the Coulomb criterion, the pore collapse model predicts that a porosity cluster collapses when the stress field in its vicinity attains the critical state according to the Coulomb criterion, which results into a linear dependence of the differential stress Q at the yield point C* with the effective stress P (Baud et al., 2015). Although our yield caps that include P* appear linear, further microstructural analysis need to be done to identify the micromechanical process and clarify the role of pore collapse in the failure of our synthetic samples.

The pore space heterogeneities of our synthetic samples appear to influence the micromechanics of failure. Yet, we believe they do not prevent us from discussing the relative influence of bulk porosity on the compactive yield behavior. A compilation of six yield envelopes for synthetic samples of porosity of 0.25 and 0.30 and of mean grain diameter of 0.2, 0.5 and 1.15 mm is presented in Figure 12. All of the compactive yield caps are linearly shaped with a negative slope. Overall, we observed that, for a given grain diameter, increasing porosity decreases the stress at which C* occurs and that a difference in porosity of 0.01 results in a difference in C* of

598 approximately 8% +/- 5%. This appears to apply whatever the grain diameter is in the range
599 0.15-1.3 mm. Indeed, at an effective pressure of 60 MPa, an increase of porosity from 0.26 to
600 0.30 (+0.04), decreases the stress at which C* occurs from 59 to 43 MPa (-28%), 97 to 70 MPa (-
601 28%) and from 147 to 95 MPa (-35%) for mean grain diameter of 1.15, 0.5 and 0.2 mm,
602 respectively.

603 As for porosity, grain size was experimentally identified to have a first-order control on
604 compactive yield of porous siliciclastic rock (Wong, 1990; Wong et al., 1992, 1997; Zhang et al.,
605 1990) and has been included as a parameter in micromechanical models (e.g., Sammis & Ashby,
606 1986; Zhang et al., 1990). In the Hertzian fracture model of Zhang et al. (1990), average grain
607 radius acts as a scaling parameter for the critical pressure P* with an equal weight than porosity.
608 This model was successfully applied to a number of natural and synthetic sandstones and
609 unconsolidated materials (David et al., 1998; Wong et al., 1997) with some scatter. However,
610 although a consensus on the key influence of grain size has been reached, compactive yield caps
611 compilations for sandstones often only discuss the influence of porosity. Figure 13 shows a
612 compilation of compactant failure caps for Boise and Bleurswiller sandstones (data from Cheung
613 et al., 2012) and sintered samples that only differ from one another in terms of their average
614 grain diameter. If we consider only the yield caps of the synthetic samples, we observe that, all
615 else being equal, an increase in average grain diameter from 0.2 to 0.5 mm (+130%) or from 0.5
616 to 1.15 mm (+150%) shifts the stress at which C* occurs to values approximately 2 times lower
617 (-50%) (Figure 13). Moreover, the difference in C* that results from a change in grain diameter
618 remains approximately the same whatever the porosity. Thus, our data show that an increase in
619 average grain diameter by a factor of 2 results in a decrease in the stress to reach C* of
620 approximately 50 +/- 5%. As for Boise and Bleurswiller sandstone, they are similar in
621 mineralogy and porosity but, although both their grain diameter distributions present a peak at
622 125 μm, the former has a wider sorting that extends up to 725 μm. Despite significantly different
623 grain sorting, their compactive yield caps for the onset of shear-enhanced compaction are very
624 similar, albeit slightly different in shape with a more linear cap for Bleurswiller sandstone. The
625 caps of our synthetics are similar in shape to those of the natural sandstones but are mapped out
626 at very different stress states (Figure 11). Tembe et al. (2008) reported that Bentheim sandstone,
627 although similar to Boise and Bleurswiller sandstones in terms of porosity, presents a compactive
628 yield cap characterized by higher stresses. Indeed, the abundance of secondary minerals (feldspar,

oxide and mica) in Boise and Bleurswiller compared to Bentheim (>99% quartz) likely causes the decrease in the compactive yield stresses for Boise and Bleurswiller sandstones. Similarly, since Bleurswiller and Boise sandstones present a grain diameter distribution with a peak at 125 μm, we would expect their compactive yield caps to be mapped out at higher stresses than the caps for the synthetic samples that have grain diameter distributions with peaks at 200, 500 and 1150 μm (Figure 13). The discrepancy in compactive yield stresses between Boise and Bleurswiller sandstones and the synthetic samples can be attributed neither to porosity nor to grain size, but possibly to the presence of cement and of secondary minerals other than quartz (feldspar, oxide and mica).

Overall, we varied grain diameter by one order of magnitude (Figure 11) and we see a large effect of that variation on the yield compactive strength of our synthetic samples. Grain diameters of natural sandstones can also vary by more than one order magnitude (Nelson & Kibler, 2003), but the effect of that variation has not hitherto been deconvolved from other microstructural factors. We thus conclude that, if grain size were to be accounted for quantitatively, its effect would be similar to that of porosity. However, we observe, for the range of porosity and grain diameter used herein, that the influence of porosity on compactive yield is higher than the influence of grain diameter. Indeed, to cover a similar range in the stress space, the average grain diameter of our synthetic samples was increased by up to 600 % (relative to the lowest range we used, 0.15-0.25 mm) while bulk porosity was only increased by up to 120% (relative to the lowest porosity we used, 0.18).

6.4 Compaction localization

For all of our synthetic samples deformed in the regime of shear-enhanced compaction, mechanical data show stress drops of variable amplitude (Figure 5), suggesting that compaction localization took place (Baud et al., 2004; Heap et al., 2015b; Louis et al., 2006). This observation concurs with the general consensus that microstructural homogeneity promote strain localization in granular materials (Katsman et al., 2005; Louis et al., 2009; Wang et al., 2005). Indeed, Cheung et al. (2012) demonstrated that uniform grain size distribution promotes the development of discrete compaction bands. As our synthetic samples are characterized by a monodisperse distribution of grain size, we expected compactant deformation to localize in the form of compaction bands. In Figure 10(c) and Figure 10(d), we juxtaposed a SEM micrograph

of a discrete compaction band in a synthetic sample and a micrograph of a discrete compaction band in Bentheim (from Baud et al., 2004), respectively. The compaction bands present very similar microstructural attributes (Figure 10(c)(d)). An important difference is that our micrograph has been obtained on a sample of porosity of 0.35. To our knowledge, the range of porosity over which compaction bands were reported in sandstones is approximately 0.13; 0.29 (Fossen et al., 2011; Schultz et al., 2010; Tembe et al., 2008). The mechanical behavior of sandstones with a porosity higher than 0.29 at or near the brittle-ductile transition has been studied (e.g., Bedford et al., 2019; Cheung et al., 2012; Wong et al., 1997) but high-porosity sandstones typically used in laboratory often have polydisperse distributions of grain size (see for example, Boise sandstone), which has been recognized to inhibit strain localization. Therefore, the effect of porosity on the propensity for compaction localization may have been masked by the influence of other structural parameters. Our new data therefore extend the upper limit of porosity for which compaction localization has been observed to 0.35 and suggest that compaction localization can occur in samples with a porosity up to 0.38 (the highest porosity of our set of samples).

However, although numerical simulations suggested compaction localization could occur in sand packs (Marketos & Bolton, 2009), experimental validation for the formation of compaction bands in high-porosity granular aggregates such as unconsolidated sands has not been reported. For example, Hangx and Brantut (2019) performed triaxial experiments on Ottawa quartz sand with a porosity of 0.36 and did not observe strain localization in the compactant regime of deformation. These authors proposed that the possibility for grain rotation and rearrangement – permitted by the lack of cementation – allows grain failure to be accommodated and prevents stress concentration to occur. Although our high-porosity synthetic samples do not have cement, we show that they can develop compaction bands in the regime of shear-enhanced compaction. Therefore, we speculate that the necks formed at grain contacts during sintering in our synthetic samples act as the cement in consolidated sandstones and play a key role in controlling compaction localization. To a first-order, the potential for compaction localization appears to be controlled not by porosity, but by the granular/non-granular and/or unconsolidated/consolidated nature of rock, which is intimately related to the degree of cementation at grain contacts and by extension, in some cases, to porosity (Lemée & Guéguen, 1996). Additionally, if we consider that the porosity of a loose packing of grains is approximately 0.38 +/- 0.01 (Johnson & Plona,

1982), the observation of discrete compaction bands in a synthetic sample of porosity of 0.35 suggests that even a small proportion of consolidated/cemented grain contacts could be sufficient to trigger stress concentrations within aggregates and the formation of compaction bands.

7 Crustal implications and concluding remarks

Crustal rocks such as sandstones and tuffs, the primary microstructural elements of which are comparable with our synthetic samples, occur as geological units in reservoirs, aquifers, fault zones and in volcanic environments; settings where they typically undergo structural changes due to geologic processes. Therefore, implications – and applications – of our results for natural systems are broad. For example, in the context of hydrocarbon and/or geothermal reservoirs, depletion-induced reservoir compaction is an ubiquitous phenomenon that eventually leads to surface subsidence (Gambolati et al., 2006; Nagel, 2001). On assessing which sedimentary layer compacts first and/or to the highest extent, unconsolidated upper formations and clay-rich formations are usually considered as the best candidates. However, reservoir formations are often only vaguely described as coarse- or fine-grained and grain size is rarely considered in numerical terms (Sun et al., 2018b), even in geotechnical models predicting the extent of irreversible compaction for the bulk reservoir (Buscarnera et al., 2020; Hol et al., 2018). Our new data suggest that formations with large grain diameters, alongside those with a high porosity, could be prime candidates for mechanical compaction and should therefore be considered when assessing reservoir subsidence.

In volcanic contexts, inelastic compaction of edifice-forming rock (including non-volcanic basement rocks) presumably acts as a driving force in the growth and destruction life-cycle of large volcanoes (Bakker et al., 2015; Concha-Dimas et al., 2005; Heap et al., 2015c; Van Wyk De Vries & Borgia, 1996), which involves episodes of spreading that eventually leads to catastrophic collapses (Van Wyk De Vries & Francis, 1997). Since flank and/or edifice collapse models often invoke a weak/ductile internal or basal unit to explain instability and collapse (Ablay & Hürlimann, 2000; Morgan & McGovern, 2005; Voight, 2000), it is important to understand what controls the mechanical behavior of porous rocks, especially considering that porous volcanic rocks can also develop compaction bands (Heap et al., 2015b, 2020). Our synthetic materials could help understand whether simple empirical or theoretical models can effectively describe the relationship between grain size, porosity and compactive yield strength,

and thus give accurate predictions for the evolution of inelastic compaction and subsequent subsidence and/or edifice spreading. Moreover, since our synthetic samples consist of a very simplified two-phase medium, such laws can be easily tested against discrete element method simulations of reservoir compaction (Alassi et al., 2006; Sun et al., 2018a) or volcanic collapses (Harnett et al., 2018) for example.

Our approach has allowed us to study the influence of deconvolved microstructural attributes on mechanical compaction. The set of mechanical and microstructural data we present show that the failure mode of analog samples made of sintered glass beads transit from brittle at low confinement to ductile with shear-enhanced compaction at high confinement. Compactive yield caps are mapped out on a range of stress states comparable to those for natural crustal rocks (the porosity and grain diameter of which are similar to those of our synthetic samples, i.e., 0.18-0.38 and 0.2-1.15 mm, respectively) and are linearly shaped when P* is known and are likely linearly shaped for the porosity-grain diameter combinations for which P* could not be measured (due to the pressure limit of the triaxial apparatus). Qualitatively speaking, mechanical and microstructural data are very similar between the natural and synthetic samples. Regarding the influence of porosity and grain size, we arrived at the following main conclusions. First, increasing only porosity or only grain diameter decreases the stress at which the onset of shear-enhanced compaction C* occurs. Second, to increase the stress at C* by 50%, porosity has to be decreased – in isolation – by 0.06 (30% relative to the range 0.18-0.38) whereas average grain diameter has to be decreased – in isolation – by 0.50 mm (53% relative to the 0.2-1.15 mm). Although the influence of porosity can be regarded as higher than the influence of grain size, our study demonstrates that, over the investigated range of porosity and grain diameter, they both exert a first-order control on the mechanical compaction of natural crustal rocks, which can span over a much broader range of porosity and grain diameters. Therefore, alongside porosity, grain diameter should become a routinely measured structural parameter when dealing with the mechanical compaction of natural crustal rocks.

Overall, we believe our study demonstrates the great suitability of sintered glass beads as crustal rock analogs and the great opportunity they embody for studying microstructural parameters such as porosity and average grain diameter in isolation. Since mixtures of glass beads of different diameters can be prepared, variably polydisperse sintered samples can be synthesized and used to investigate the influence of grain size distribution and polydispersivity on

mechanical and hydraulic behavior. Further, the addition of cement and/or other materials to the glass bead mixtures could also be considered in order to sharpen our understanding of the deconvolved influence of microstructural parameters on the mechanical and hydraulic properties of crustal rocks.

Acknowledgments and Data

This paper has benefitted from constructive reviews by Douglas Schmitt, Sergey Stanchits and one anonymous reviewer. Jérôme Fortin, Mai-linh Doan, Jérémie Vasseur and Dominique de Ligny are thanked for the discussions. The authors thank Bertrand Renaudié for the preparation of the samples and Gilles Morvan for his assistance using the SEM. The first author acknowledges funding from the Doctoral School at the University of Strasbourg.The data supporting the manuscript's analysis and conclusions is available at https://doi.org/10.6084/m9.figshare.13208192 .

References

Ablay, G., & Hürlimann, M. (2000). Evolution of the north flank of Tenerife by recurrent giant landslides. *Journal of Volcanology and Geothermal Research*, 103(1–4), 135–159. https://doi.org/10.1016/S0377-0273(00)00220-1

Alassi, H. T. I., Li, L., & Holt, R. M. (2006). Discrete Element Modeling of Stress and Strain Evolution Within and Outside a Depleting Reservoir. *Pure and Applied Geophysics*, 163, 1131–1151. https://doi.org/10.1007/3-7643-7712-7_13

Atapour, H., & Mortazavi, A. (2018). The influence of mean grain size on unconfined compressive strength of weakly consolidated reservoir sandstones. *Journal of Petroleum Science and Engineering*, 171, 63–70. https://doi.org/10.1016/j.petrol.2018.07.029

Atkinson, B. K., & Meredith, P. G. (1987). Experimental fracture mechanics data for rocks and minerals. In Fracture mechanics of rock (pp. 477–519). Academic Press Inc.(London) Ltd.

Bakker, R. R., Violay, M. E. S., Benson, P. M., & Vinciguerra, S. C. (2015). Ductile flow in sub-volcanic carbonate basement as the main control for edifice stability: new experimental insights. *Earth and Planetary Science Letters*, 430, 533–541.

Bansal, N. P., & Doremus, R. H. (2013). Handbook of Glass Properties. Handbook of Glass Properties, 1–680. https://doi.org/10.1016/C2009-0-21785-5

780 Baud, P., Klein, E., & Wong, T. (2004). Compaction localization in porous sandstones: spatial
781 evolution of damage and acoustic emission activity. *Journal of Structural Geology*, 26(4),
782 603–624. https://doi.org/10.1016/j.jsg.2003.09.002

783 Baud, P., Vajdova, V., & Wong, T. (2006). Shear-enhanced compaction and strain localization:
784 Inelastic deformation and constitutive modeling of four porous sandstones. *Journal of*
785 *Geophysical Research: Solid Earth*, 111(B12), n/a-n/a.
786 https://doi.org/10.1029/2005JB004101

787 Baud, P., Wong, T., & Zhu, W. (2014). Effects of porosity and crack density on the compressive
788 strength of rocks. *International Journal of Rock Mechanics and Mining Sciences*, 67,
789 202–211. https://doi.org/10.1016/j.ijrmms.2013.08.031

790 Baud, P., Reuschlé, T., Ji, Y., Cheung, C. S. N., & Wong, T. (2015). Mechanical compaction and
791 strain localization in Bleurswiller sandstone. *Journal of Geophysical Research: Solid*
792 *Earth*, 120(9), 6501–6522. https://doi.org/10.1002/2015JB012192

793 Baud, P., Exner, U., Lommatzsch, M., Reuschlé, T., & Wong, T. (2017). Mechanical behavior,
794 failure mode, and transport properties in a porous carbonate. Journal of Geophysical
795 Research: Solid Earth, 122(9), 7363–7387. https://doi.org/10.1002/2017JB014060

796 Bedford, J. D., Faulkner, D. R., Wheeler, J., & Leclère, H. (2019). High-Resolution Mapping of
797 Yield Curve Shape and Evolution for High-Porosity Sandstone. *Journal of Geophysical*
798 *Research: Solid Earth*, 124(6), 5450–5468. https://doi.org/10.1029/2018JB016719

799 Berge, P. A., Bonner, B. P., & Berryman, J. G. (1995). Ultrasonic velocity-porosity relationships
800 for sandstone analogs made from fused glass beads. *GEOPHYSICS*, 60(1), 108–119.
801 https://doi.org/10.1190/1.1443738

802 Bernabé, Y., Mok, U., & Evans, B. (2003). Permeability-porosity Relationships in Rocks
803 Subjected to Various Evolution Processes. Thermo-Hydro-Mechanical Coupling in
804 Fractured Rock, 160, 937–960. https://doi.org/10.1007/978-3-0348-8083-1_9

805 Bjørlykke, K. (2006). Effects of compaction processes on stresses, faults, and fluid flow in
806 sedimentary basins: Examples from the Norwegian margin. *Geological Society Special*
807 *Publication*, 253(1), 359–379. https://doi.org/10.1144/GSL.SP.2006.253.01.19

808 Blair, S. C., Berge, P. A., & Berryman, J. G. (1993). Two-point correlation functions to
809 characterize microgeometry and estimate permeabilities of synthetic and natural
810 sandstones. Livermore, CA: Lawrence Livermore National Laboratory (LLNL).
811 https://doi.org/10.2172/10182383

812 Bloch, S., Lander, R. H., & Bonnell, L. (2002). Anomalously High Porosity and Permeability in
813 Deeply Buried Sandstone Reservoirs: Origin and Predictability. *The American*
814 *Association of Petroleum Geologists*, 86(2), 301–328.
815 https://doi.org/10.1306/61EEDABC-173E-11D7-8645000102C1865D

816 de Bono, J., McDowell, G., & Wanatowski, D. (2015). Investigating the micromechanics of
817 cemented sand using DEM. *International Journal for Numerical and Analytical Methods*
818 *in Geomechanics*, 39(6), 655–675. https://doi.org/10.1002/nag.2340

819 Bourbie, T., & Zinszner, B. (1985). Hydraulic and Acoustic Properties as a Function of Porosity
820 in Fontainebleau Sandstone. *Journal of Geophysical Research*, 90(4), 524–532.

821 Bouzidi, Y., & Schmitt, D. R. (2012). Incidence-angle-dependent acoustic reflections from
822 liquid-saturated porous solids. *Geophysical Journal International*, 191(3), 1427–1440.
823 https://doi.org/10.1111/j.1365-246X.2012.05695.x

824 den Brok, S. W. J., David, C., & Bernabé, Y. (1997). Preparation of synthetic sandstones with
825 variable cementation for studying the physical properties of granular rocks. Comptes
826 Rendus de l'Académie Des Sciences - Series IIA - *Earth and Planetary Science*, 325(7),
827 487–492. https://doi.org/10.1016/S1251-8050(97)89866-7

828 Buscarnera, G., Chen, Y., Lizárraga, J., & Zhang, R. (2020). Multi-scale simulation of rock
829 compaction through breakage models with microstructure evolution. *Proceedings of the*
830 *International Association of Hydrological Sciences*, 382, 421–425.
831 https://doi.org/10.5194/piahs-382-421-2020

832 Caruso, L., Simmons, G., & Wilkens, R. (1985). The physical properties of a set of sandstones-
833 Part I. The samples. *International Journal of Rock Mechanics and Mining Sciences And*,
834 22(6), 381–392. https://doi.org/10.1016/0148-9062(85)90003-8

835 Castagna, J. P., & Backus, M. M. (1993). Offset-Dependent Reflectivity—Theory and Practice
836 of AVO Analysis. (Castagna, Ed.), Offset-Dependent Reflectivity—Theory and Practice

837 of AVO Analysis. Society of Exploration Geophysicists.
838 https://doi.org/10.1190/1.9781560802624

839 Chang, C., Zoback, M. D., & Khaksar, A. (2006). Empirical relations between rock strength and
840 physical properties in sedimentary rocks. *Journal of Petroleum Science and Engineering*,
841 51(3–4), 223–237. https://doi.org/10.1016/j.petrol.2006.01.003

842 Chapman, S., Quintal, B., Holliger, K., Baumgartner, L., & Tisato, N. (2018). Laboratory
843 measurements of seismic attenuation and Young's modulus dispersion in a partially and
844 fully water-saturated porous sample made of sintered borosilicate glass. *Geophysical*
845 *Prospecting*, 66(7), 1384–1401. https://doi.org/10.1111/1365-2478.12643

846 Cheung, C. S. N., Baud, P., & Wong, T. (2012). Effect of grain size distribution on the
847 development of compaction localization in porous sandstone. *Geophysical Research*
848 *Letters*, 39(21), n/a-n/a. https://doi.org/10.1029/2012GL053739

849 Concha-Dimas, A., Cerca, M., Rodríguez, S. R., & Watters, R. J. (2005). Geomorphological
850 evidence of the influence of pre-volcanic basement structure on emplacement and
851 deformation of volcanic edifices at the Cofre de Perote-Pico de Orizaba chain and
852 implications for avalanche generation. *Geomorphology*, 72(1–4), 19–39.
853 https://doi.org/10.1016/j.geomorph.2005.05.004

854 Dardis, O., & Mccloskey, J. (1998). Permeability porosity relationships from numerical
855 simulations of fluid flow. *Geophysical Research Letters*, 25(9), 1471–1474.

856 David, C., Menéndez, B., & Bernabé, Y. (1998). The mechanical behaviour of synthetic
857 sandstone with varying brittle cement content. *International Journal of Rock Mechanics*
858 *and Mining Sciences*, 35(6), 759–770. https://doi.org/10.1016/S0148-9062(98)00003-5

859 Doyen, P. M. (1988). Permeability, conductivity, and pore geometry of sandstone. *Journal of*
860 *Geophysical Research*, 93(B7), 7729–7740. https://doi.org/10.1029/JB093iB07p07729

861 Eberhart-Phillips, D., Han, D., & Zoback, M. D. (1989). Empirical relationships among seismic
862 velocity, effective pressure, porosity, and clay content in sandstone. *Geophysics*, 54(1),
863 82–89.

Fabre, D., & Gustkiewicz, J. (1997). Poroelastic properties of limestones and sandstones under hydrostatic conditions. *International Journal of Rock Mechanics and Mining Sciences*, 34(1), 127–134. https://doi.org/10.1016/S1365-1609(97)80038-X

Farquharson, J. I., Baud, P., & Heap, M. J. (2017). Inelastic compaction and permeability evolution in volcanic rock. *Journal of Geophysical Research: Solid Earth*, 8(2), 561–581. https://doi.org/10.5194/se-8-561-2017

Fortin, J., Schubnel, A., & Guéguen, Y. (2005). Elastic wave velocities and permeability evolution during compaction of Bleurswiller sandstone. *International Journal of Rock Mechanics and Mining Sciences*, 42(7-8 SPEC. ISS.), 873–889. https://doi.org/10.1016/j.ijrmms.2005.05.002

Fortin, J., Stanchits, S., Dresen, G., & Guéguen, Y. (2006). Acoustic emission and velocities associated with the formation of compaction bands in sandstone. *Journal of Geophysical Research: Solid Earth*, 111(10), 1–16. https://doi.org/10.1029/2005JB003854

Fossen, H., Schultz, R. A., & Torabi, A. (2011). Conditions and implications for compaction band formation in the Navajo Sandstone, Utah. *Journal of Structural Geology*, 33(10), 1477–1490. https://doi.org/10.1016/j.jsg.2011.08.001

Frenkel, J. (1945). Viscous flow of crystalline bodies under the action of surface tension. *Journal of Physics*, 9, 385.

Gambolati, G., Ferronato, M., & Teatini, P. (2006). Reservoir compaction and land subsidence. Revue Européenne de Génie Civil, 10(6–7), 731–762. https://doi.org/10.1080/17747120.2006.9692854

Ghazvinian, E., Diederichs, M. S., & Quey, R. (2014). 3D random Voronoi grain-based models for simulation of brittle rock damage and fabric-guided micro-fracturing. *Journal of Rock Mechanics and Geotechnical Engineering*, 6(6), 506–521. https://doi.org/10.1016/j.jrmge.2014.09.001

Grunder, A., & Russell, J. K. (2005). Welding processes in volcanology: Insights from field, experimental, and modeling studies. *Journal of Volcanology and Geothermal Research*, 142(1-2 SPEC. ISS.), 1–9. https://doi.org/10.1016/j.jvolgeores.2004.10.010

892 Guéguen, Y., & Boutéca, M. (2004). Mechanics of fluid saturated rocks. Elsevier Academic
893 Press.

894 Guéguen, Y., & Fortin, J. (2013). Elastic envelopes of porous sandstones. *Geophysical Research*
895 *Letters*, 40(14), 3550–3555. https://doi.org/10.1002/grl.50676

896 Guyon, E., Oger, L., & Plona, T. J. (1987). Transport properties in sintered porous media
897 composed of two particle sizes. *Journal of Physics D: Applied Physics*, 20(12), 1637–
898 1644. https://doi.org/10.1088/0022-3727/20/12/015

899 Haeri, S. M., Hosseini, S. M., Toll, D. G., & Yasrebi, S. S. (2005). The behaviour of an
900 artificially cemented sandy gravel. *Geotechnical and Geological Engineering*, 23(5),
901 537–560. https://doi.org/10.1007/s10706-004-5110-7

902 Hangx, S. J. T., & Brantut, N. (2019). Micromechanics of High-Pressure Compaction in
903 Granular Quartz Aggregates. *Journal of Geophysical Research: Solid Earth*, 124(7),
904 6560–6580. https://doi.org/10.1029/2018JB016494

905 Harnett, C. E., Thomas, M. E., Purvance, M. D., & Neuberg, J. (2018). Using a discrete element
906 approach to model lava dome emplacement and collapse. *Journal of Volcanology and*
907 *Geothermal Research*, 359, 68–77. https://doi.org/10.1016/j.jvolgeores.2018.06.017

908 Heap, M. J., & Wadsworth, F. B. (2016). Closing an open system: Pore pressure changes in
909 permeable edifice rock at high strain rates. *Journal of Volcanology and Geothermal*
910 *Research*, 315, 40–50. https://doi.org/10.1016/J.JVOLGEORES.2016.02.011

911 Heap, M. J., Farquharson, J. I., Baud, P., Lavallée, Y., & Reuschlé, T. (2015c). Fracture and
912 compaction of andesite in a volcanic edifice. *Bulletin of Volcanology*, 77(6).
913 https://doi.org/10.1007/s00445-015-0938-7

914 Heap, M. J., Kennedy, B. M., Pernin, N., Jacquemard, L., Baud, P., Farquharson, J. I., et al.
915 (2015a). Mechanical behaviour and failure modes in the Whakaari (White Island volcano)
916 hydrothermal system, New Zealand. *Journal of Volcanology and Geothermal Research*,
917 295, 26–42. https://doi.org/10.1016/j.jvolgeores.2015.02.012

Heap, M. J., Brantut, N., Baud, P., & Meredith, P. G. (2015b). Time-dependent compaction band formation in sandstone. *Journal of Geophysical Research: Solid Earth*, 120(7), 4808–4830. https://doi.org/10.1002/2015JB012022

Heap, M. J., Kushnir, A. R. L., Gilg, H. A., Wadsworth, F. B., Reuschlé, T., & Baud, P. (2017). Microstructural and petrophysical properties of the Permo-Triassic sandstones (Buntsandstein) from the Soultz-sous-Forêts geothermal site (France). *Geothermal Energy*, 5(1), 26. https://doi.org/10.1186/s40517-017-0085-9

Heap, M. J., Baud, P., McBeck, J. A., Renard, F., Carbillet, L., & Hall, S. A. (2020). Imaging strain localisation in porous andesite using digital volume correlation. *Journal of Volcanology and Geothermal Research*, 404, 107038. https://doi.org/10.1016/j.jvolgeores.2020.107038

Hol, S., Van Der Linden, A., Bierman, S., Marcelis, F., & Makurat, A. (2018). Rock Physical Controls on Production-induced Compaction in the Groningen Field. *Scientific Reports*, 8(1), 7156. https://doi.org/10.1038/s41598-018-25455-z

Johnson, D. L., & Plona, T. J. (1982). Acoustic slow waves and the consolidation transition. The *Journal of the Acoustical Society of America*, 72(2), 556–565. https://doi.org/10.1121/1.388036

Katsman, R., Aharonov, E., & Scher, H. (2005). Numerical simulation of compaction bands in high-porosity sedimentary rock. *Mechanics of Materials*, 37(1), 143–162. https://doi.org/10.1016/j.mechmat.2004.01.004

Klein, E., Baud, P., Reuschlé, T., & Wong, T. (2001). Mechanical behaviour and failure mode of Bentheim sandstone under triaxial compression. *Physics and Chemistry of the Earth, Part A: Solid Earth and Geodesy*, 26(1–2), 21–25. https://doi.org/10.1016/S1464-1895(01)00017-5

Krohn, C. E. (1988). Sandstone fractal and Euclidean pore volume distributions. *Journal of Geophysical Research*, 93(B4), 3286. https://doi.org/10.1029/JB093iB04p03286

Kuczynski, G. C. (1949). Study of the Sintering of Glass. *Journal of Applied Physics*, 20(12), 1160–1163. https://doi.org/10.1063/1.1698291

946 Lemée, C., & Guéguen, Y. (1996). Modeling of porosity loss during compaction and
947 cementation of sandstones. *Geology*, 24(10), 875. https://doi.org/10.1130/0091-
948 7613(1996)024

949 Lindquist, W. B., Venkatarangan, A., Dunsmuir, J. R., & Wong, T. (2000). Pore and throath size
950 distributions measured from synchrotron X-ray tomographic images of Fontainebleau
951 sandstones. *Journal of Geophysical Research*, 105(B9), 509–521.

952 Louis, L., Wong, T., Baud, P., & Tembe, S. (2006). Imaging strain localization by X-ray
953 computed tomography: discrete compaction bands in Diemelstadt sandstone. *Journal of*
954 *Structural Geology*, 28(5), 762–775. https://doi.org/10.1016/j.jsg.2006.02.006

955 Louis, L., Baud, P., & Wong, T. (2007). Characterization of pore-space heterogeneity in
956 sandstone by X-ray computed tomography. *Geological Society Special Publication*, 284,
957 127–146. https://doi.org/10.1144/SP284.9

958 Louis, L., Baud, P., & Rolland, A. (2009). Compaction localization in high porosity sandstones
959 with various degrees of heterogeneity : insight from X-ray computed tomography. In
960 ROCKENG09: Proceedings of the 3rd CANUS Rock Mechanics Symposium (Vol. 2009,
961 pp. 1–2).

962 Mackenzie, J. K., & Shuttleworth, R. (1949). A Phenomenological Theory of Sintering.
963 *Proceedings of the Physical Society*. Section B, 62(12), 833.
964 https://doi.org/10.1088/0370-1301/62/12/310

965 Marketos, G., & Bolton, M. D. (2009). Compaction bands simulated in Discrete Element Models.
966 *Journal of Structural Geology*, 31(5), 479–490. https://doi.org/10.1016/j.jsg.2009.03.002

967 Menéndez, B., Zhu, W., & Wong, T. (1996). Micromechanics of brittle faulting and cataclastic
968 flow in Berea sandstone. *Journal of Structural Geology*, 18(1), 1–16.
969 https://doi.org/10.1016/0191-8141(95)00076-P

970 Morgan, J. K., & McGovern, P. J. (2005). Discrete element simulations of gravitational volcanic
971 deformation: 1. Deformation structures and geometries. *Journal of Geophysical Research:*
972 *Solid Earth*, 110(5), 1–22. https://doi.org/10.1029/2004JB003252

973 Nagel, N. B. (2001). Compaction and subsidence issues within the petroleum industry: From
974 Wilmington to Ekofisk and beyond. *Physics and Chemistry of the Earth, Part A: Solid*
975 *Earth and Geodesy*, 26(1–2), 3–14. https://doi.org/10.1016/S1464-1895(01)00015-1

976 Nelson, P. H., & Kibler, J. E. (2003). A Catalog of Porosity and Permeability from Core Plugs in
977 Siliciclastic Rocks. Retrieved from https://pubs.usgs.gov/of/2003/ofr-03-420/ofr-03-
978 420.html#References

979 Olsson, W. A. (1999). Theoretical and experimental investigation of compaction bands in porous
980 rock. *Journal of Geophysical Research: Solid Earth*, 104(B4), 7219–7228.
981 https://doi.org/10.1029/1998jb900120

982 Papadopoulos, L., Porter, M. A., Daniels, K. E., Bassett, D. S., & Estrada, E. (2018). Network
983 analysis of particles and grains. *Journal of Complex Networks*, 6(4), 485–565.
984 https://doi.org/10.1093/comnet/cny005

985 Paterson, M. S., & Wong, T. (2005). Experimental Rock Deformation: The Brittle Field, 2nd
986 Edition. Springer Verlag.

987 Plona, T. J. (1980). Observation of a second bulk compressional wave in a porous medium at
988 ultrasonic frequencies. *Applied Physics Letters*, 36(4), 259–261.
989 https://doi.org/10.1063/1.91445

990 Quane, S. L., Russell, J. K., & Friedlander, E. A. (2009). Time scales of compaction in volcanic
991 systems. *Geology*, 37(5), 471–474. https://doi.org/10.1130/G25625A.1

992 Rogers, J. J. W., & Head, W. B. (1961). Relationships Between Porosity, Median Size, and
993 Sorting Coefficients of Synthetic Sands. *Journal of Sedimentary Research*, Vol. 31(3),
994 467–470. https://doi.org/10.1306/74d70ba5-2b21-11d7-8648000102c1865d

995 Rutter, E. H., & Glover, C. T. (2012). The deformation of porous sandstones; are Byerlee friction
996 and the critical state line equivalent? *Journal of Structural Geology*, 44, 129–140.
997 https://doi.org/10.1016/j.jsg.2012.08.014

998 Saadi, F. A., Wolf, K.-H., & van Kruijsdijk, C. (2017). Characterization of Fontainebleau
999 Sandstone: Quartz Overgrowth and its Impact on Pore-Throat Framework. *Journal of*
1000 *Petroleum & Environmental Biotechnology*, 08(03). https://doi.org/10.4172/2157-
1001 7463.1000328

1002 Sammis, C. G., & Ashby, M. F. (1986). The failure of brittle porous solids under compressive
1003 stress states. *Acta Metallurgica*, 34(3), 511–526. https://doi.org/10.1016/0001-
1004 6160(86)90087-8

1005 Scherer, M. (1987). Parameters influencing porosity in sandstones: a model for sandstone
1006 porosity prediction. *American Association of Petroleum Geologists Bulletin*, 71(5), 485–
1007 491. https://doi.org/10.1306/94886ed9-1704-11d7-8645000102c1865d

1008 Schöpfer, M. P. J., Abe, S., Childs, C., & Walsh, J. J. (2009). The impact of porosity and crack
1009 density on the elasticity, strength and friction of cohesive granular materials: Insights
1010 from DEM modelling. International *Journal of Rock Mechanics and Mining Sciences*,
1011 46(2), 250–261. https://doi.org/10.1016/j.ijrmms.2008.03.009

1012 Schultz, R. A., Okubo, C. H., & Fossen, H. (2010). Porosity and grain size controls on
1013 compaction band formation in Jurassic Navajo Sandstone. *Geophysical Research Letters*,
1014 37(22), n/a-n/a. https://doi.org/10.1029/2010GL044909

1015 Scott, T. E., & Nielsen, K. C. (1991). The effects of porosity on the brittle-ductile transition in
1016 sandstones. *Journal of Geophysical Research*, 96(90), 405–414.

1017 Selley, R. C. (2004). Sedimentary Rocks: Mineralogy and classification. In Encyclopedia of
1018 Geology (pp. 25–37). Elsevier Inc. https://doi.org/10.1016/B0-12-369396-9/00304-X

1019 Sternlof, K. R., Rudnicki, J. W., & Pollard, D. D. (2005). Anticrack inclusion model for
1020 compaction bands in sandstone. *Journal of Geophysical Research: Solid Earth*, 110(B11),
1021 1–16. https://doi.org/10.1029/2005JB003764

1022 Sulem, J., & Ouffroukh, H. (2006). Hydromechanical behaviour of Fontainebleau sandstone.
1023 *Rock Mechanics and Rock Engineering*, 39(3), 185–213. https://doi.org/10.1007/s00603-
1024 005-0065-4

1025 Sun, Z., Tang, H., Espinoza, D. N., Balhoff, M. T., & Killough, J. E. (2018a). Discrete element
1026 modeling of grain crushing and implications on reservoir compaction. Journal of
1027 *Petroleum Science and Engineering*, 171, 431–439.
1028 https://doi.org/10.1016/j.petrol.2018.07.046

1029 Sun, Z., Tang, H., Espinoza, D. N., Balhoff, M. T., & Killough, J. E. (2018b). Pore-to reservoir-
1030 scale modeling of depletion-induced compaction and implications on production rate.

1031 Proceedings - SPE Annual Technical Conference and Exhibition, 2018-Septe(Ostermeier
1032 1995). https://doi.org/10.2118/191390-ms

1033 Taylor, S. K., Nicol, A., & Walsh, J. J. (2008). Displacement loss on growth faults due to
1034 sediment compaction. Journal of Structural *Geology*, 30(3), 394–405.
1035 https://doi.org/10.1016/j.jsg.2007.11.006

1036 Tembe, S., Vajdova, V., Wong, T., & Zhu, W. (2006). Initiation and propagation of strain
1037 localization in circumferentially notched samples of two porous sandstones. *Journal of*
1038 *Geophysical Research: Solid Earth*, 111(2). https://doi.org/10.1029/2005JB003611

1039 Tembe, S., Baud, P., & Wong, T. (2008). Stress conditions for the propagation of discrete
1040 compaction bands in porous sandstone. *Journal of Geophysical Research: Solid Earth*,
1041 113(9), 1–16. https://doi.org/10.1029/2007JB005439

1042 Torquato, S. (2002). Random Heterogeneous Materials: Microstructure and Macroscopic
1043 Properties (Springer).

1044 Van Wyk De Vries, B., & Borgia, A. (1996). The role of basement in volcano deformation.
1045 *Geological Society Special Publication*, 110(1), 95–110.
1046 https://doi.org/10.1144/GSL.SP.1996.110.01.07

1047 Van Wyk De Vries, B., & Francis, P. W. (1997). Catastrophic collapse at stratovolcanoes
1048 induced by gradual volcano spreading. *Nature*, 387(6631), 387–390.
1049 https://doi.org/10.1038/387387a0

1050 Vasseur, J., Wadsworth, F. B., Lavallée, Y., & Dingwell, D. B. (2016). Dynamic elastic moduli
1051 during isotropic densification of initially granular media. *Geophysical Journal*
1052 *International*, 204(3), 1721–1728. https://doi.org/10.1093/gji/ggv550

1053 Voight, B. (2000). Structural stability of andesite volcanoes and lava domes. *Philosophical*
1054 *Transactions of the Royal Society A: Mathematical, Physical and Engineering Science*s,
1055 358(1770), 1663–1703. https://doi.org/10.1098/rsta.2000.0609

1056 Wadsworth, F. B., Vasseur, J., Llewellin, E. W., Schauroth, J., Dobson, K. J., Scheu, B., &
1057 Dingwell, D. B. (2016). Sintering of viscous droplets under surface tension. *Proceedings*
1058 *of the Royal Society A: Mathematical, Physical and Engineering Science*, 472(2188),
1059 20150780. https://doi.org/10.1098/rspa.2015.0780

1060 Wadsworth, F. B., Vasseur, J., Llewellin, E. W., Dobson, K. J., Colombier, M., Von Aulock, F.
1061 W., et al. (2017). Topological inversions in coalescing granular media control fluid-flow
1062 regimes. *Physical Review E*, 96(3), 33113. https://doi.org/10.1103/PhysRevE.96.033113

1063 Wadsworth, F. B., Vasseur, J., Schauroth, J., Llewellin, E. W., Dobson, K. J., Havard, T., et al.
1064 (2019). A general model for welding of ash particles in volcanic systems validated using
1065 in situ X-ray tomography. *Earth and Planetary Science Letters*, 525, 115726.
1066 https://doi.org/10.1016/j.epsl.2019.115726

1067 Walsh, J. B. (1965). Effect of Cracks on the Compressibility of Rocks. *Journal of Geophysical*
1068 *Research*, 70(2), 381–389. https://doi.org/10.1029/JB083iB09p04459

1069 Wang, B. S., Chen, Y., & Wong, T. (2005). Compaction localization in porous sandstone:
1070 Acoustic emission activity, microstructural development and discrete element simulation.
1071 In 11th International Conference on Fracture 2005, ICF11 (Vol. 4, pp. 2421–2424).

1072 Wasantha, P. L. P., Ranjith, P. G., Zhao, J., Shao, S. S., & Permata, G. (2015). Strain Rate Effect
1073 on the Mechanical Behaviour of Sandstones with Different Grain Sizes. *Rock Mechanics*
1074 *and Rock Engineering*, 48(5), 1883–1895. https://doi.org/10.1007/s00603-014-0688-4

1075 Weng, M.-C., & Li, H.-H. (2012). Relationship between the deformation characteristics and
1076 microscopic properties of sandstone explored by the bonded-particle model. International
1077 *Journal of Rock Mechanics and Mining Sciences*, 56, 34–43.
1078 https://doi.org/10.1016/J.IJRMMS.2012.07.003

1079 Winkler, K. W. (1985). Dispersion analysis of velocity and attenuation in Berea sandstone.
1080 *Journal of Geophysical Research*, 90(B8), 6793.
1081 https://doi.org/10.1029/jb090ib08p06793

1082 Wong, T. (1990). Mechanical compaction and the brittle-ductile transition in porous sandstones.
1083 *Geological Society Special Publication*, 54, 111–122.
1084 https://doi.org/10.1144/GSL.SP.1990.054.01.12

1085 Wong, T., & Baud, P. (1999). Mechanical compaction of porous sandstone. *Oil and Gas Science*
1086 *and Technology*, 54(6), 715–727. https://doi.org/10.2516/ogst:1999061

1087 Wong, T., & Baud, P. (2012). The brittle-ductile transition in porous rock: A review. *Journal of*
1088 *Structural Geology*, 44, 25–53. https://doi.org/10.1016/j.jsg.2012.07.010

1089 Wong, T., Szeto, H., & Zhang, J. (1992). Effect of loading path and porosity on the failure mode
1090 of porous rocks. *Applied Mechanics Reviews*, 45(8), 281–293.
1091 https://doi.org/10.1115/1.3119759

1092 Wong, T., David, C., & Zhu, W. (1997). The transition from brittle faulting to cataclastic flow in
1093 porous sandstones: Mechanical deformation. *Journal of Geophysical Research: Solid*
1094 *Earth*, 102(B2), 3009–3025. https://doi.org/10.1029/96JB03281

1095 Wong, T., Baud, P., & Klein, E. (2001). Localized failure modes in a compactant porous rock.
1096 *Geophysical Research Letters*, 28(13), 2521–2524.
1097 https://doi.org/10.1029/2001GL012960

1098 Xu, T., Fu, T. F., Heap, M. J., Meredith, P. G., Mitchell, T. M., & Baud, P. (2020). Mesoscopic
1099 Damage and Fracturing of Heterogeneous Brittle Rocks Based on Three-dimensional
1100 Polycrystalline Discrete Element Method. *Rock Mechanics and Rock Engineering*, 1–21.
1101 https://doi.org/10.1007/s00603-020-02223-y

1102 Yin, H., & Dvorkin, J. (1994). Strength of cemented grains. *Geophysical Research Letters*,
1103 21(10), 903–906. https://doi.org/10.1029/93GL03535

1104 Zhang, J., Wong, T.-F., & Davis, D. M. (1990). Micromechanics of pressure-induced grain
1105 crushing in porous rocks. *Journal of Geophysical Research*, 95(B1), 341.
1106 https://doi.org/10.1029/JB095iB01p00341

1107 Zhu, W., Baud, P., & Wong, T. (2010). Micromechanics of cataclastic pore collapse in limestone.
1108 *Journal of Geophysical Research: Solid Earth*, 115(4).
1109 https://doi.org/10.1029/2009JB006610

1110 Zhu, W., Baud, P., Vinciguerra, S., & Wong, T. (2011). Micromechanics of brittle faulting and
1111 cataclastic flow in Alban Hills tuff. *Journal of Geophysical Research: Solid Earth*,
1112 116(6), 1–23. https://doi.org/10.1029/2010JB008046

1113

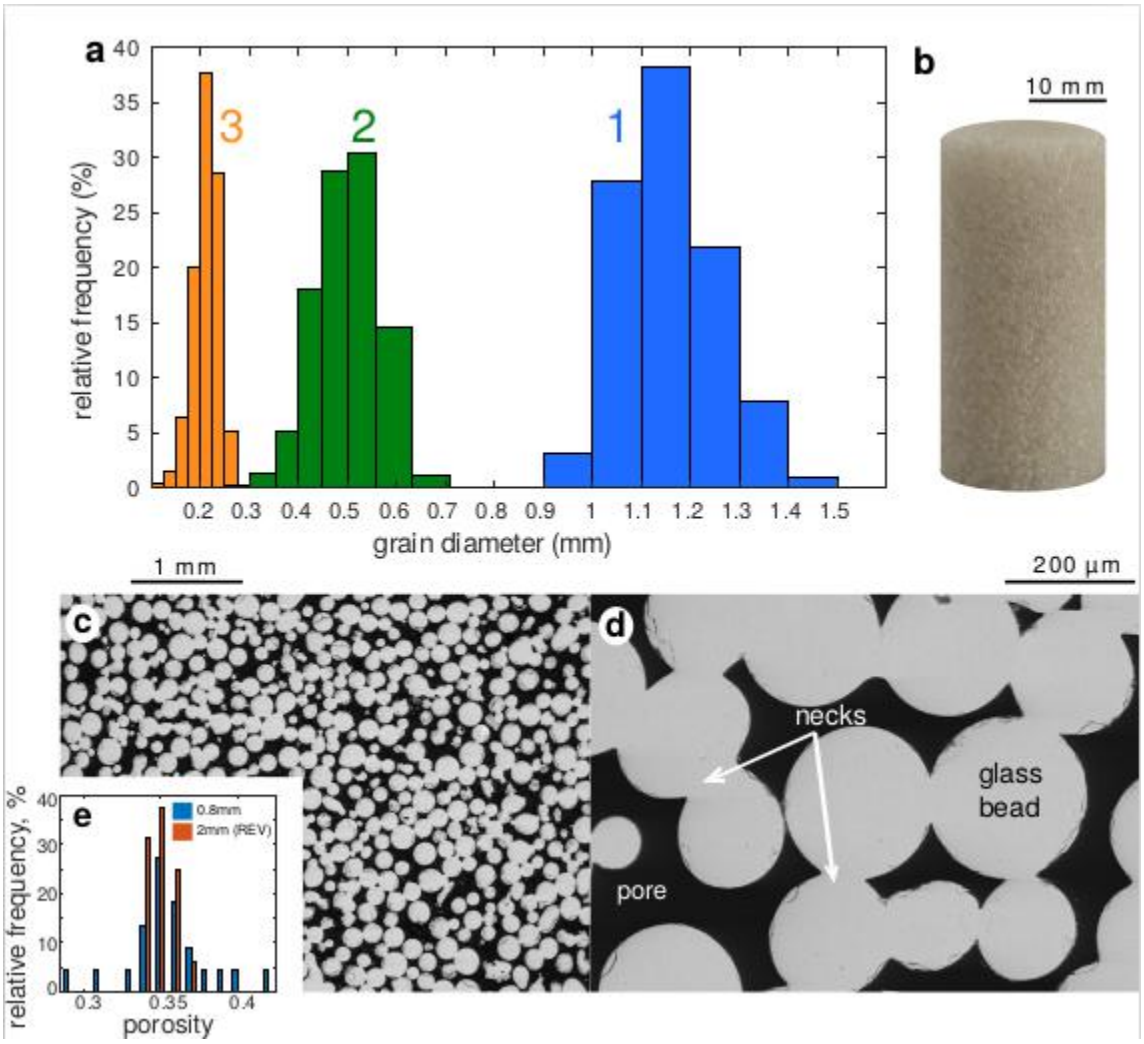

Figure 1. Microstructural description of the synthetic samples. (**a**) Grain diameter distributions corresponding to the different mean grain diameter considered, 3: 0.15-0.25 mm (orange), 2: 0.4 0.6 mm (green), 1: 1.0-1.3 mm (blue). Although these distributions are not technically monodisperse but monomodal, we herein use the term monodisperse to describe our samples. (**b**) Photograph of a synthetic sample with a porosity of 0.35 and a mean grain diameter of 0.2 mm and (**c**) corresponding scanning electron micrograph of its microstructure (black: porosity, gray: glass). (**d**) Scanning electron micrograph showing the necks that have grown between initially adjacent beads during sintering. (**e**) 2D porosity distributions measured for the same sample using a window with a 0.8 mm edge-length (blue) or with a 2 mm edge-length (representative elementary volume, red) using image processing program ImageJ. Frequencies cluster around 0.35, which corresponds to the porosity measured in laboratory.

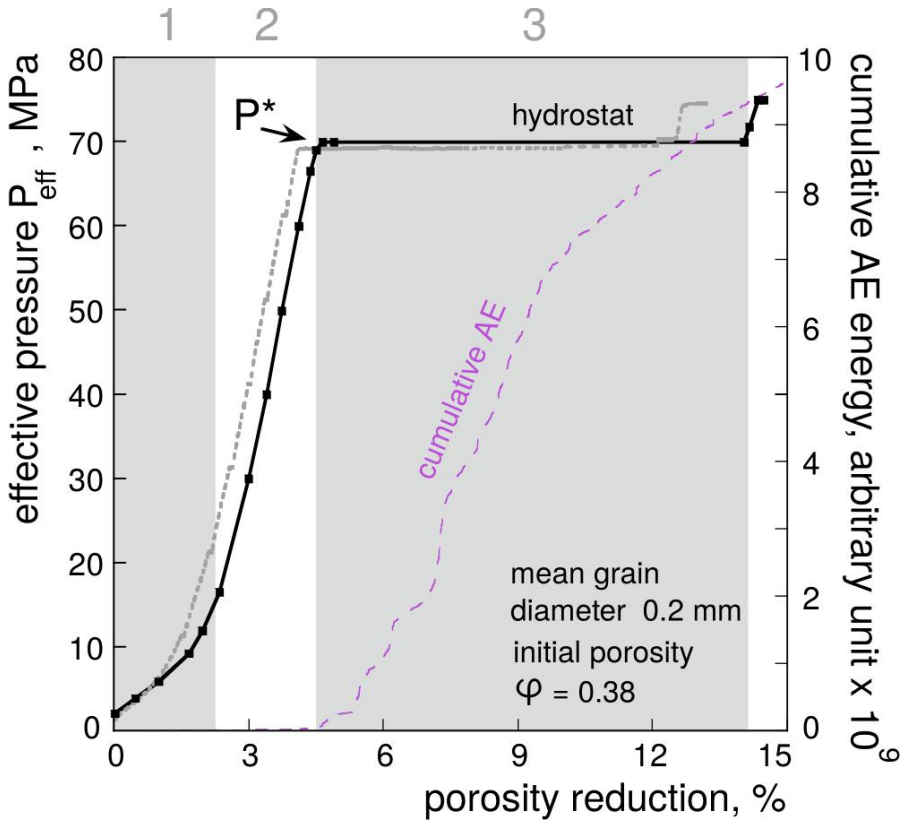

Figure 2. Representative mechanical data (black line) and cumulative acoustic emission energy (purple dashed line) for hydrostatic tests performed on the synthetic samples. These data were obtained on synthetic samples of mean grain diameter of 0.2 mm and initial porosity of 0.38. The critical stress for the onset of grain crushing P* is indicated by an arrow. The porosity reduction in percentage corresponds to the absolute loss of porosity, i.e., a porosity reduction of 14% refers to a drop from 0.38 to 0.24. (1) When P_{eff} is first increased, porosity decreases non-linearly as a result of grains rearrangements. (2) As P_{eff} is increased further, the sample undergoes elastic deformation until P_{eff} reaches the critical value P* beyond which (3) the sample porosity decreases suddenly and significantly by grain crushing (inelastic deformation).

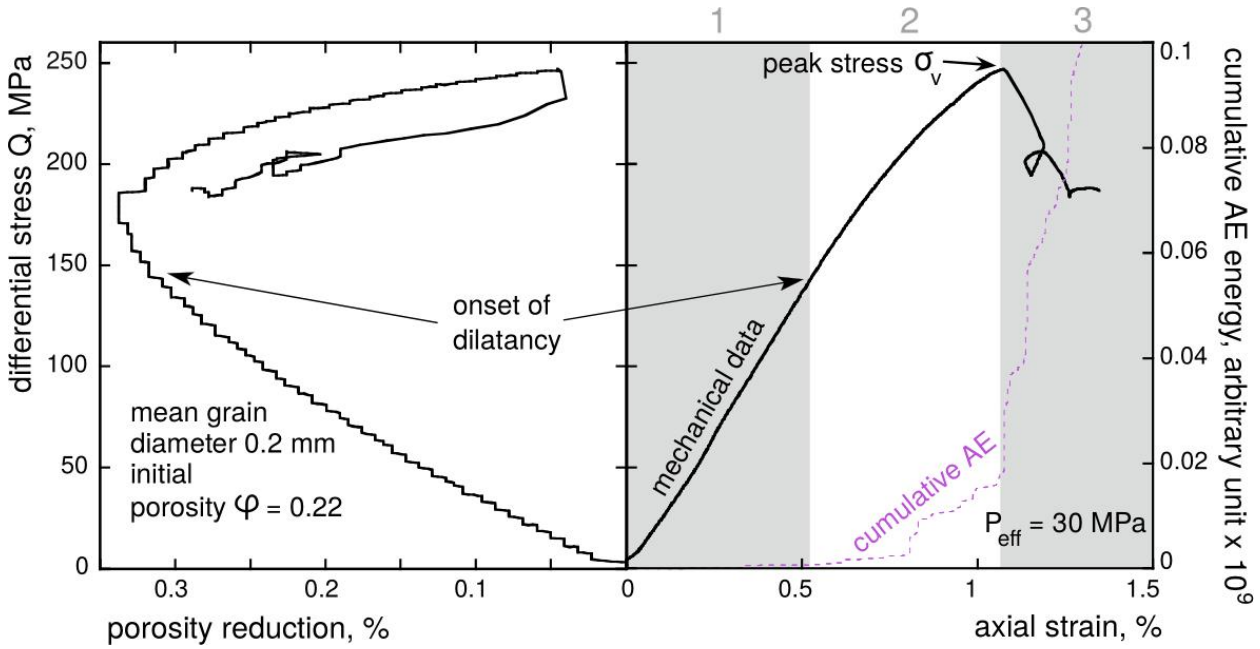

Figure 3. Representative mechanical data (black lines) and cumulative acoustic emission energy (purple dashed line) for triaxial tests performed in the brittle regime. The triaxial test presented was performed at P_{eff} = 30 MPa on a synthetic sample of mean grain diameter of 0.2 mm and initial porosity of 0.22. The peak stress σ_v is indicated by an arrow. The porosity reduction in percentage corresponds to the absolute loss of porosity, i.e., a porosity reduction of 0.4% refers to a drop from 0.22 to 0.216. (1) When loading is first applied, the sample undergoes elastic axial strain and porosity decreases linearly. (2) The transition to the inelastic stage of deformation takes place at the onset of dilatancy and, as Q is increased further, it eventually reaches (3) a critical peak stress σ_v at which point brittle failure takes place and the stress drops to a residual value.

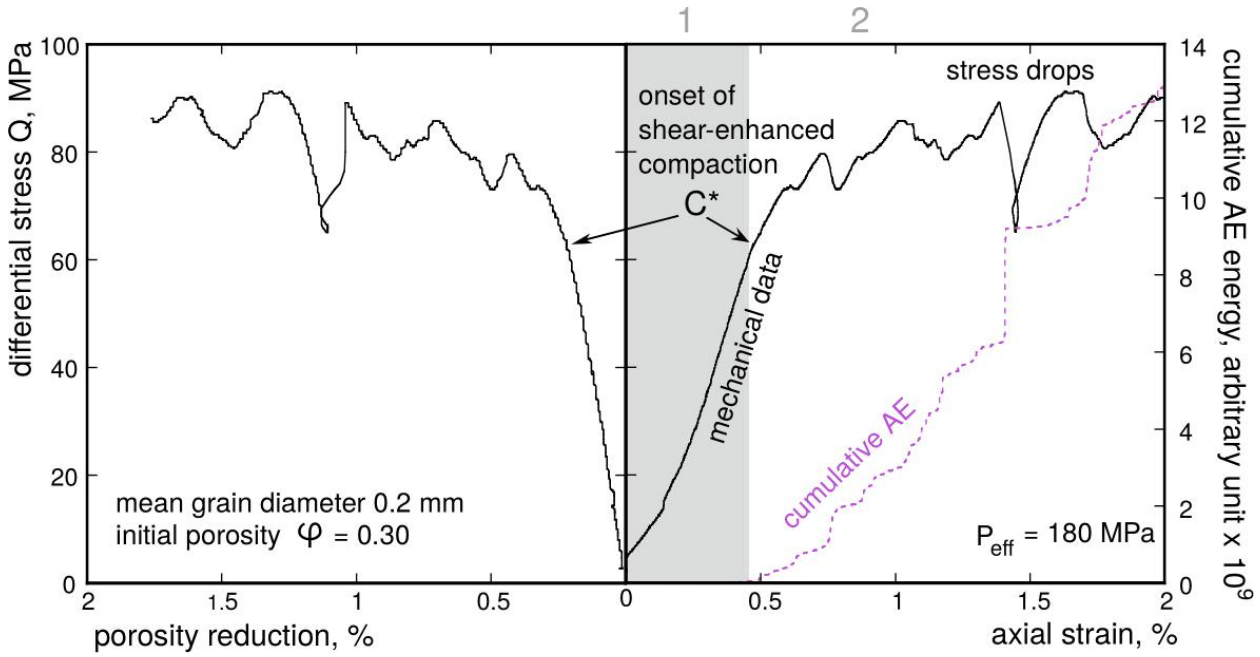

Figure 4. Representative mechanical data (black lines) and cumulative acoustic emission energy (purple dashed line) for triaxial tests performed in the regime of shear-enhanced compaction. The triaxial test presented was performed at P_{eff} = 180 MPa on a synthetic sample of mean grain diameter of 0.2 mm and initial porosity of 0.30. The critical stress for the onset of shear-enhanced compaction C* is indicated by an arrow. The porosity reduction in percentage corresponds to the absolute loss of porosity, i.e., a porosity reduction of 2% refers to a drop from 0.30 to 0.28. (1) Axial strain increases and porosity decreases linearly as loading is first applied. (2) The transition to the inelastic stage of deformation takes place as Q reaches the critical value C* for the onset of shear-enhanced compaction.

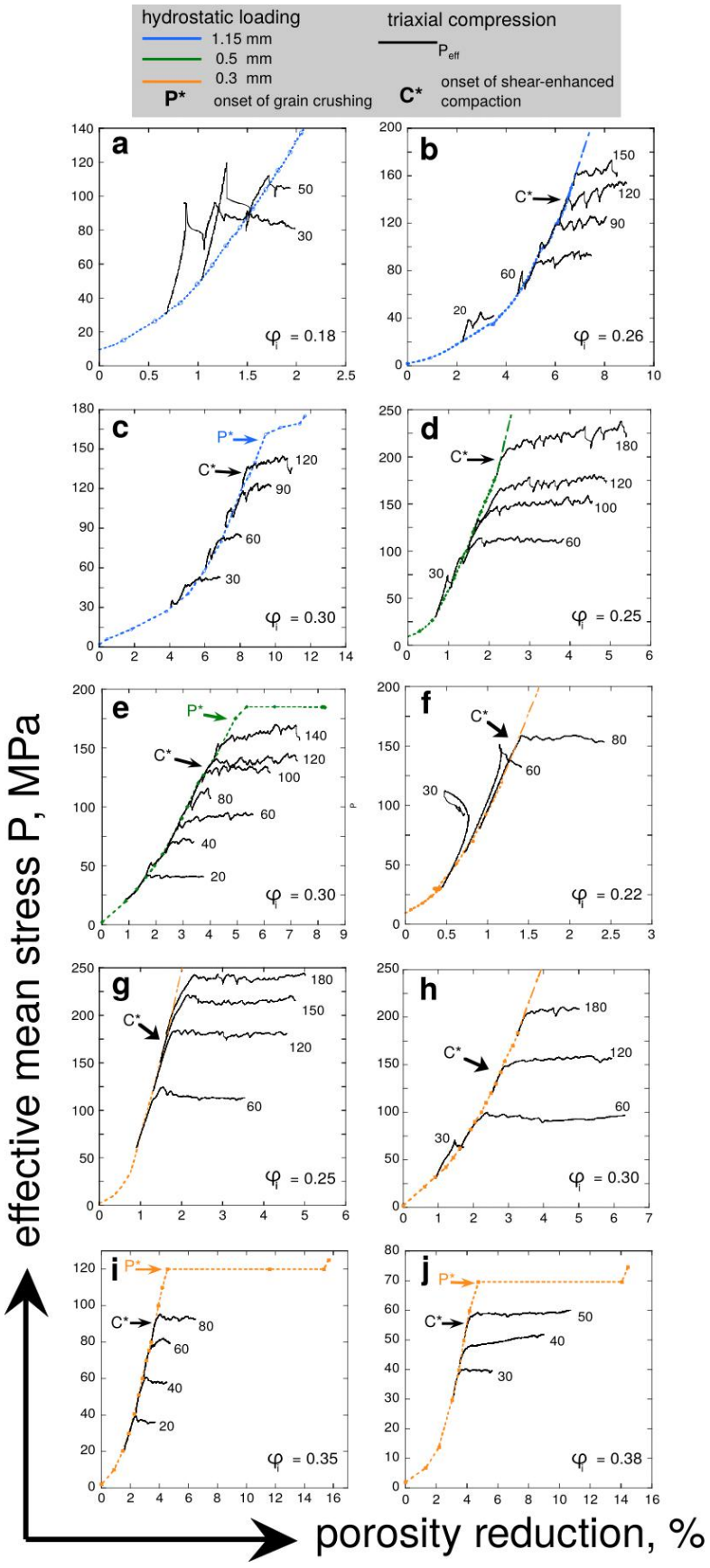
hydrostatic loading
1.15 mm
0.5 mm
0.3 mm
P* onset of grain crushing
triaxial compression
P_eff
C* onset of shear-enhanced compaction
a
b
c
d
e
f
g
h
i
j
φi = 0.18
φi = 0.26
φi = 0.30
φi = 0.25
φi = 0.30
φi = 0.22
φi = 0.25
φi = 0.30
φi = 0.35
φi = 0.38
effective mean stress P, MPa
porosity reduction, %

Figure 5. Compilations of mechanical data from hydrostatic loading (dashed colored) and triaxial tests (black) for samples with a mean grain diameter of 1.15 mm (blue) and an initial porosity of (**a**) 0.18, (**b**) 0.26 and (**c**) 0.30; a mean grain diameter of 0.5 mm (green) and an initial porosity of (**d**) 0.25 and (**e**) 0.30; and a mean grain diameter of 0.2 mm (orange) and an initial porosity of (**f**) 0.22, (**g**) 0.25, (**h**) 0.30, (**i**) 0.35 and (**j**) 0.38. Effective pressures at which triaxial tests were conducted are indicated at the end of the corresponding curves. The onset for inelastic deformation corresponds to the departure of the effective mean stress – porosity reduction curve from the hydrostat. For illustration, the onset of shear-enhanced compaction is indicated as C* by black arrows. The critical stresses P* for the onset of grain crushing are indicated by colored arrows on the hydrostats.

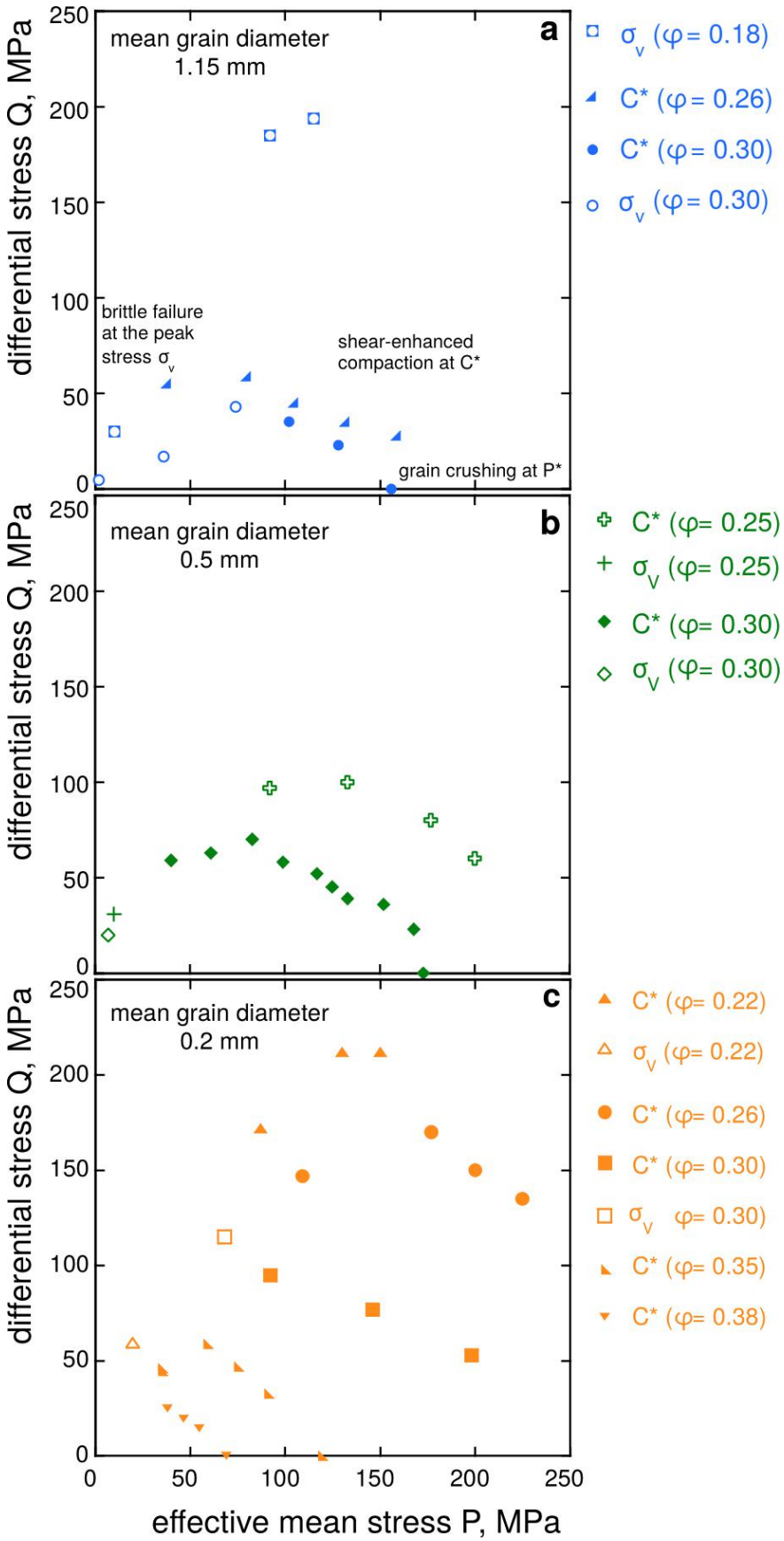
a
mean grain diameter
1.15 mm
brittle failure
at the peak
stress σv
shear-enhanced
compaction at C*
grain crushing at P*
σv (φ = 0.18)
C* (φ = 0.26)
C* (φ = 0.30)
σv (φ = 0.30)
b
mean grain diameter
0.5 mm
C* (φ= 0.25)
σV (φ= 0.25)
C* (φ= 0.30)
σV (φ= 0.30)
c
mean grain diameter
0.2 mm
C* (φ= 0.22)
σV (φ= 0.22)
C* (φ= 0.26)
C* (φ= 0.30)
σV φ= 0.30)
C* (φ= 0.35)
C* (φ= 0.38)
differential stress Q, MPa
effective mean stress P, MPa
0
50
100
150
200
250

1169 **Figure 6.** Compilations of failure envelopes for synthetic samples of mean grain diameter of (**a**)
1170 1.15 mm, (**b**) 0.5 mm and (**c**) 0.2 mm. Initial porosity of the synthetic samples is indicated in the
1171 legend. Failure envelopes are mapped out by critical stresses σ_v (brittle triaxial test), C* (ductile
1172 triaxial test) and P* (hydrostatic test). Open symbols correspond to peak stress values and solid
1173 symbols to C* values. P* (also a solid symbol) anchors the envelope to the x-axis.

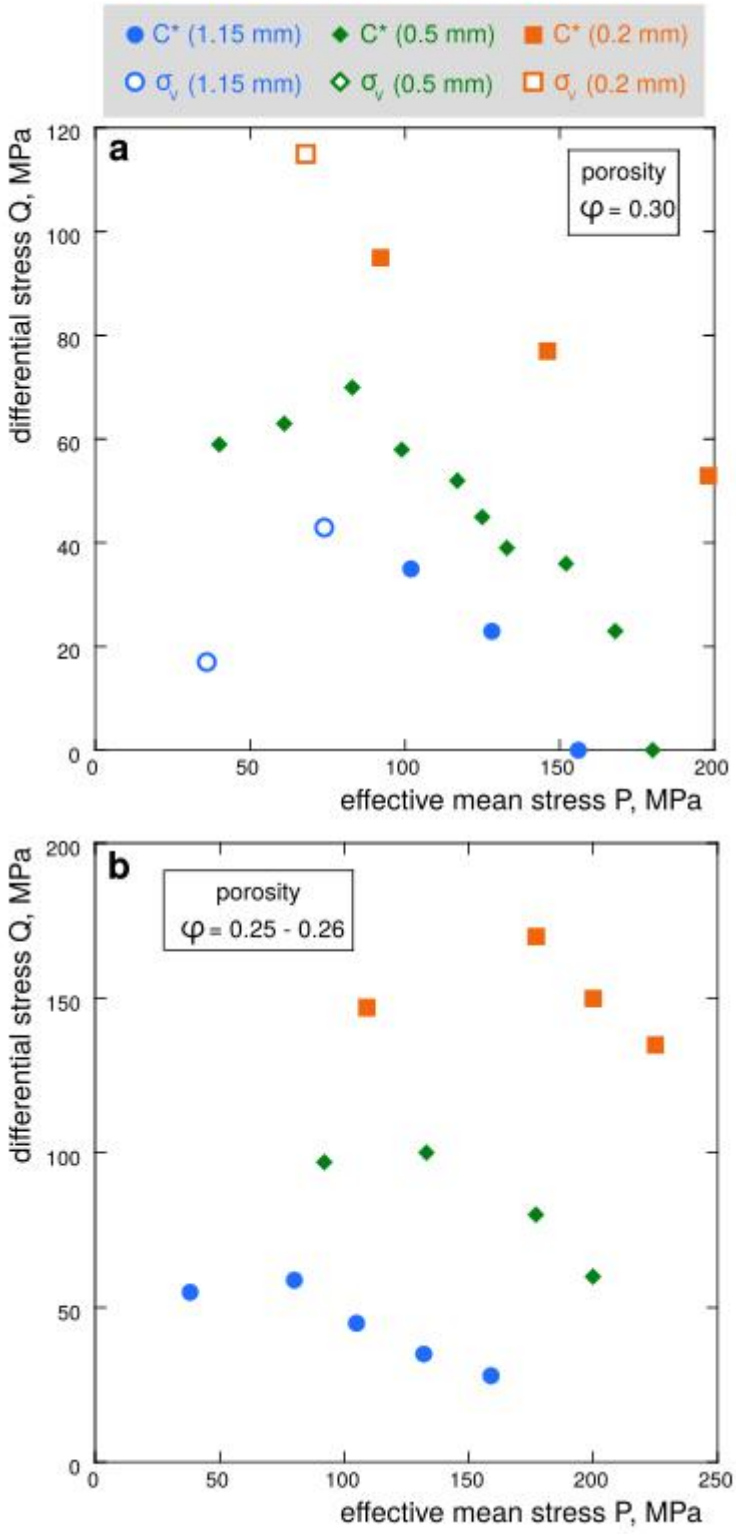
C* (1.15 mm)
C* (0.5 mm)
C* (0.2 mm)
σv (1.15 mm)
σv (0.5 mm)
σv (0.2 mm)
a
porosity
φ = 0.30
differential stress Q, MPa
effective mean stress P, MPa
b
porosity
φ = 0.25 - 0.26
differential stress Q, MPa
effective mean stress P, MPa

1174

1175 **Figure 7.** Compilations of failure envelopes for synthetic samples with a porosity of (**a**) 0.30 and
1176 (**b**) 0.25. Mean grain diameter of the synthetic samples is indicated in the legend. Failure
1177 envelopes are mapped out by critical stresses σ_v (brittle triaxial test), C* (ductile triaxial test) and
1178 P* (hydrostatic test). Open symbols correspond to peak stress values and solid symbols to C*
1179 values. P* (also a solid symbol) anchors the envelope to the x-axis.
1180

1181

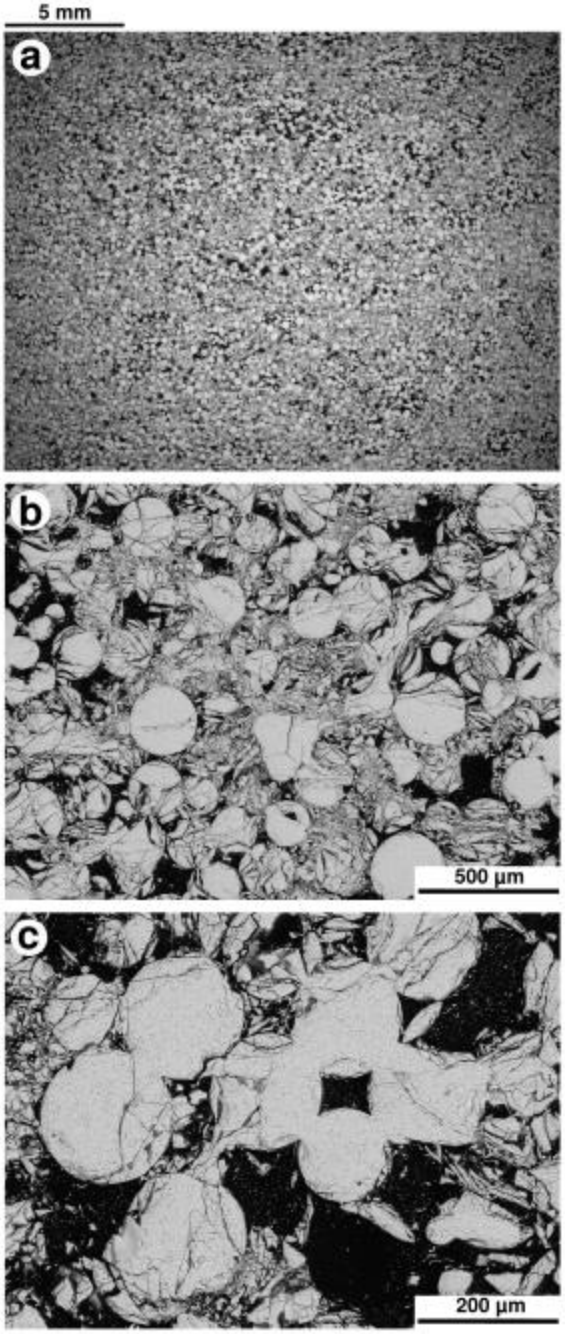

1182

1183 **Figure 8.** Representative scanning electron micrograph of the (**a**) microstructure of a synthetic
1184 sample deformed under hydrostatic loading up to an effective stress beyond P*. (**b**)(**c**) Zooms in
1185 showing extensive grain crushing. Black: porosity, gray: glass.

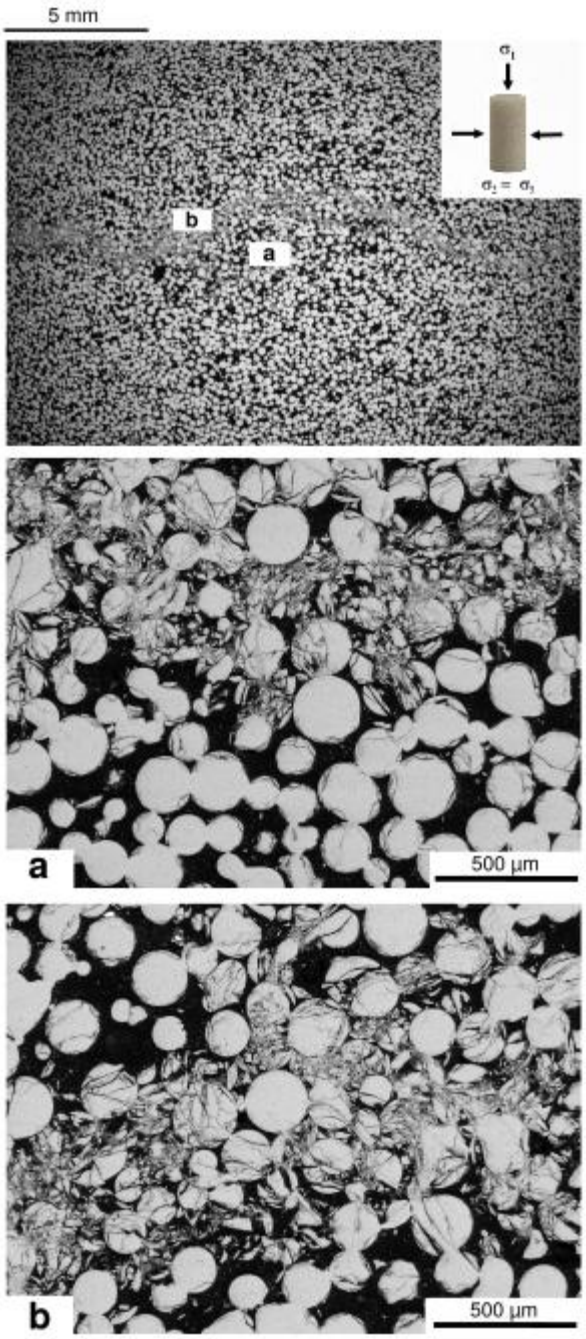

Figure 9. Scanning electron micrograph of the microstructure of a synthetic sample that failed by development of discrete compaction bands. Sample 3314, with a porosity of 0.35 and a mean grain diameter of 0.2 mm, was deformed under 80 MPa (Table 2). Overview of the thin section allows for the observation of a discrete compaction band in the middle, formed in a direction normal to the maximum principal stress σ1. (**a**) and (**b**) show micrographs of a discrete 2-5

1192 grain-thick band within which most grains are crushed. The microstructure outside of the band is
1193 almost intact. Black: porosity, gray: glass.
1194

1195

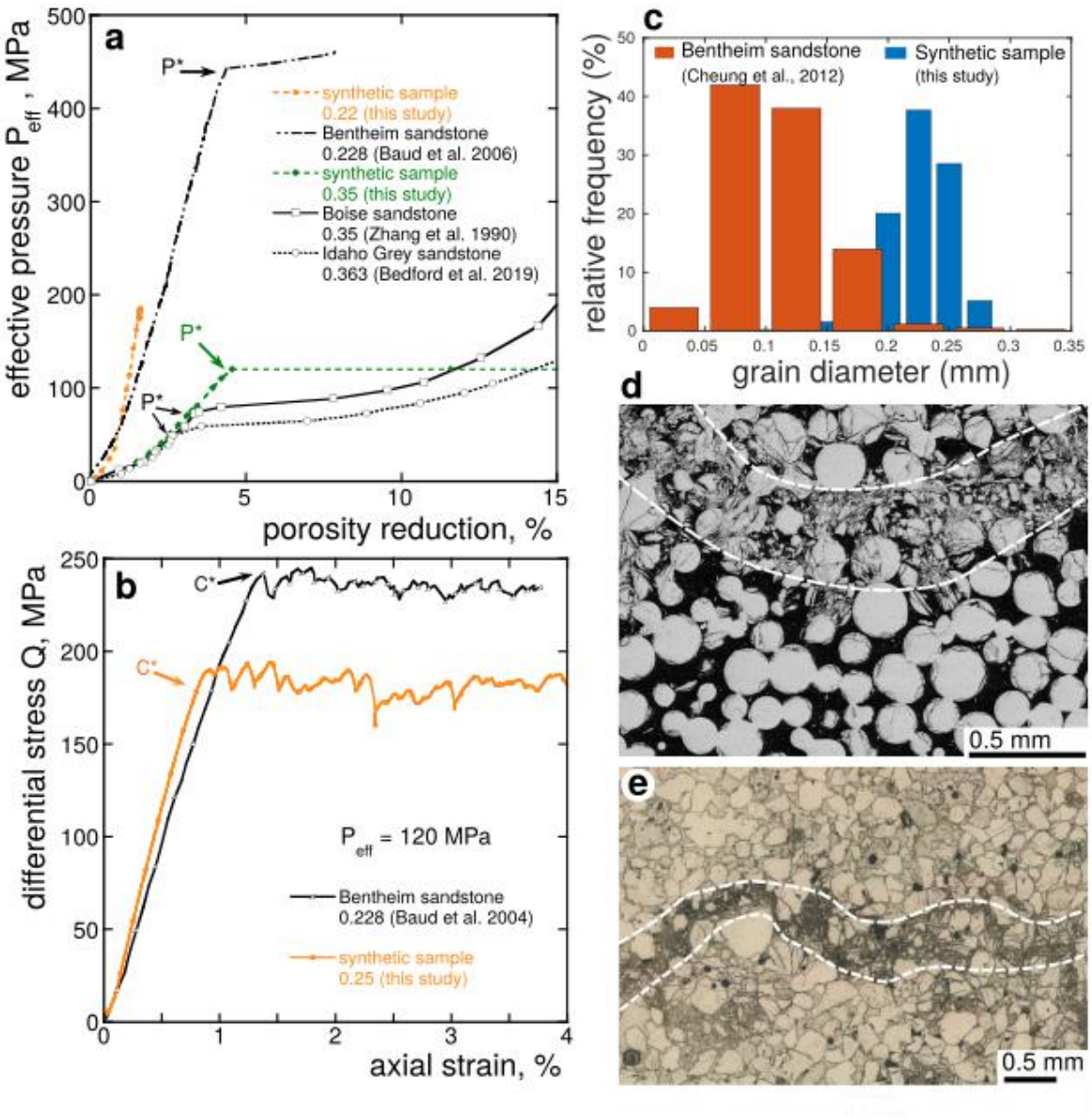

1196

1197 **Figure 10.** Data from tests performed on synthetic samples compared to data for sandstones
1198 from the literature. (**a**) Comparison of the hydrostatic loading curve of a synthetic sample (green
1199 dashed) with a porosity of 0.35 and a mean grain diameter of 0.5 mm and of the hydrostatic
1200 loading curve of a synthetic sample (orange curve) with a porosity of 0.22 and a mean grain size
1201 of 0.2 mm, with the hydrostat of Boise sandstone (black line), with a porosity of 0.35 and a mean
1202 grain diameter of 0.92 mm (Zhang et al., 1990), the hydrostat of Idaho Gray sandstone (dashed
1203 black) with a porosity of 0.363 and a mean grain diameter of 0.7 mm (Bedford et al. 2019) and

1204 the hydrostat of Bentheim sandstone with a porosity of 0.228 and a grain diameter of 0.3 mm
1205 (Baud et al., 2006). The onset of grain crushing is indicated as P*. (**b**) Comparison of stress-
1206 strain curves obtained during a triaxial test at an effective pressure of 120 MPa performed on a
1207 synthetic sample (orange line) with a porosity of 0.25 and a mean grain diameter of 0.2 mm and
1208 on Bentheim sandstone (black line)(Baud et al., 2004). The onset of shear-enhanced compaction
1209 is indicated as C*. (**c**) For reference, the smallest grain size distribution used in this study is
1210 presented along the grain size distribution of Bentheim sandstone (data from Cheung et al. 2012).
1211 (**d**) Comparison of a scanning electron micrograph of a discrete compaction band observed in a
1212 synthetic sample ($\varphi = 0.35$) and (**e**) an optical microscope image of a discrete compaction band
1213 in Bentheim sandstone ($\varphi = 0.23$; Baud et al., 2004).
1214

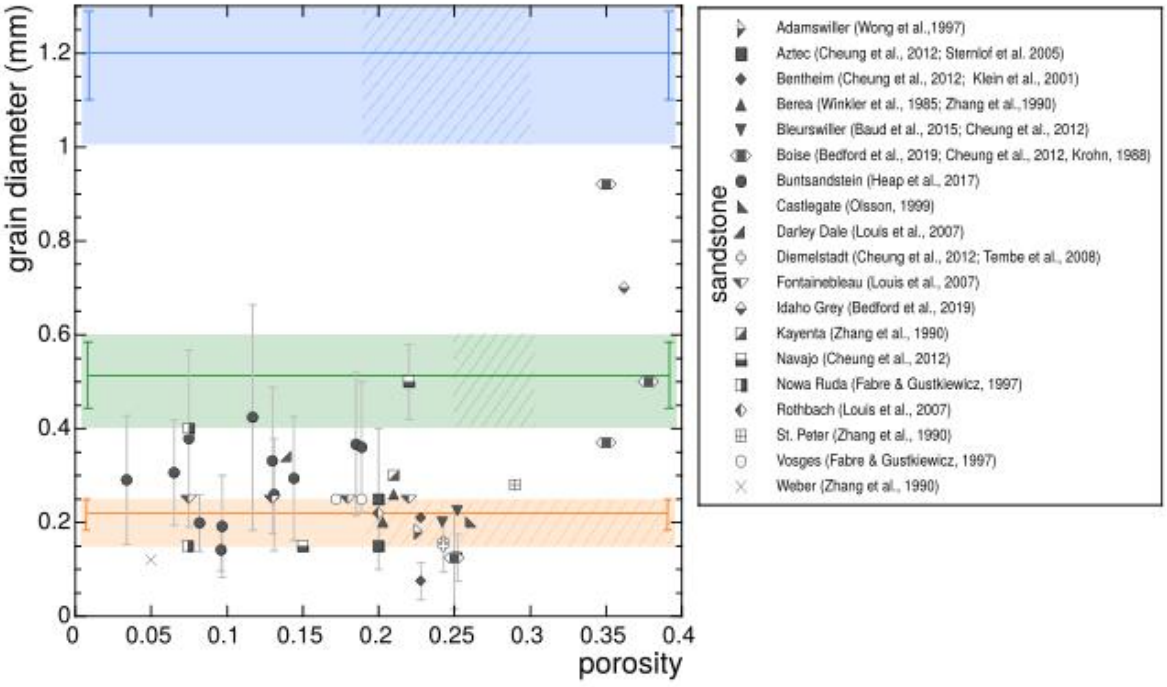

Figure 11. Compilation of porosity and grain diameter for laboratory sandstones. All data are from the literature, references are given in the legend. Colored areas correspond to the range of porosity-grain diameter accessible by sintering glass beads. The dashed areas correspond to the range we specifically investigated in this study. The error bars give the standard deviation of the grain diameter distribution, when it has been reported.

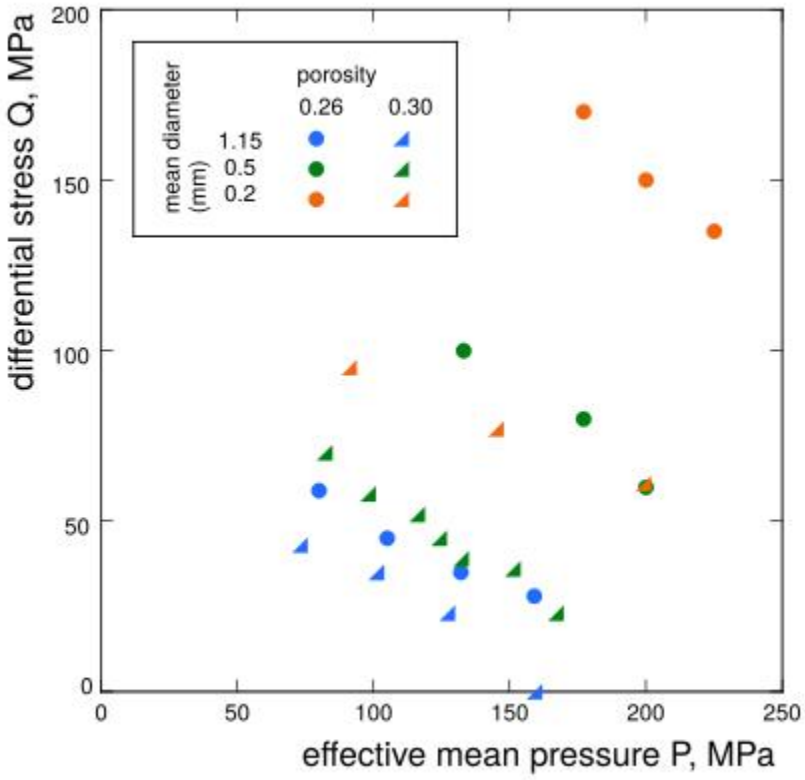

1222

1223 **Figure 12.** Influence of porosity on the compactive yield strength. Compactive yield envelopes
1224 for synthetic samples with a porosity of 0.26 (round solid symbol) or 0.30 (triangle solid symbol)
1225 and a mean grain diameter of 1.15 mm (blue), 0.5 mm (green) or 0.2 mm (orange) are compiled.

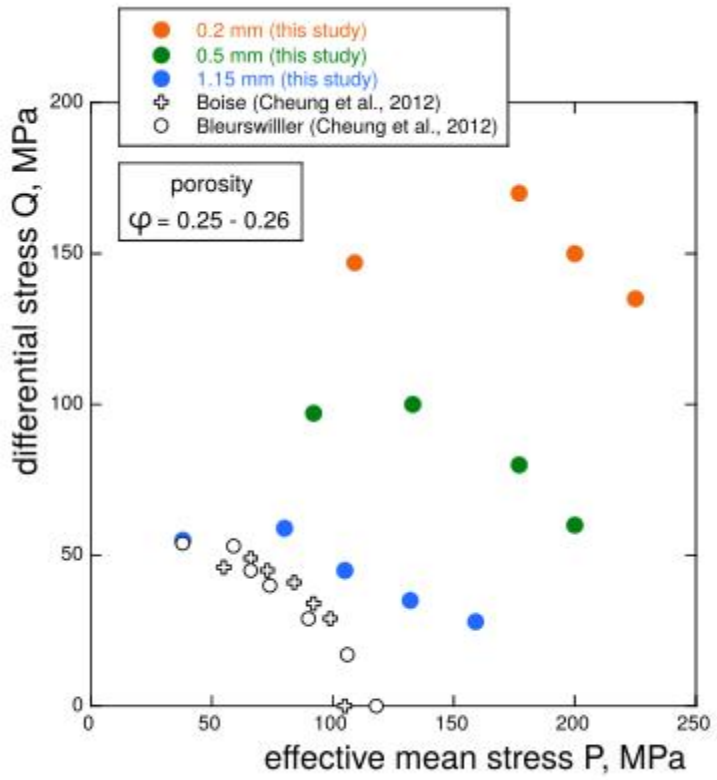

1226

1227 **Figure 13.** Influence of grain diameter on the compactive yield strength. Compactive yield
1228 envelopes for synthetic samples with a porosity of 0.25 and a mean grain diameter of 0.2 mm
1229 (orange), 0.5 mm (green) and 1.15 mm (blue) are compiled with yield envelopes for Boise (open
1230 cross) and Bleurswiller (open circle) sandstones (data from Cheung et al., 2012).